IEEE Transactions on Robotics (T-RO) paper, presented at ICRA 2024, Yokohama, Japan. Cite as T-RO paper.

Morphological Design for Pneumatic Soft Actuators and Robots with Desired Deformation Behavior

Feifei Chen, *Member, IEEE,* Zenan Song, Shitong Chen, Guoying Gu, *Senior Member, IEEE,* and Xiangyang Zhu, *Member, IEEE*

***Abstract*—A homogeneous pneumatic soft robot may generate complex output motions using a simple input pressure, resulting from its morphological shape that locally deforms the soft material to different degrees by simultaneously tailoring the structural characteristics and orienting the input pressure. To date, design of the morphological shape (inverse problem) has not been fully addressed. This article outlines a geometry-mechanics-optimization integrated approach to automatically shaping a pneumatic soft actuator or robot that achieves the desired deformation behavior. Instead of constraining the robot's geometry within any predefined regular shape, we employ B-splines to allow generation of freeform boundary surfaces, and use nonlinear mechanical modelling and shape derivative based optimization to navigate the high-dimensional design space. Our design framework can readily regulate the surface quality during the morphological evolution, by imposing the geometric constraints in terms of the principal curvatures and the minimal distance between surfaces as penalty functions. The effect of external forces including the gravity and the interaction force at the end-effector is also taken into account to generalize the method for design problems in which the load capability is also pursued. To improve the computational efficiency, sub-optimization problems are constructed within a trust region in which the displacement-dependent objective function is approximated by its first-order Taylor polynomial based on the gradient information to avoid frequently performing time-consuming nonlinear finite element analysis. The sub-optimization problems are then solved by the quasi-Newton method combined with the backtracking line search strategy. We showcase various applications to validate our design approach, including actuators for basic extension, bending, and twisting motions, and continuous robot arms that can perform desired in-plane and out-of-plane configurations. We also show that our method can address design of multiple chambers for achieving multiple target deformation behaviors, by co-optimizing the morphological shape and air pressures, which is validated by two examples.**

***Index Terms*—pneumatic soft robots, morphological design, shape optimization.**

I. Introduction

A soft elastomeric body subjected to an input pressure may deform continuously by virtue of the inherent compliance. This simple yet effective physical principle has lent itself to the widely used pneumatic actuation in soft robots, enabling applications ranging from artificial muscles [1], [2] to versatile grippers [3], [4] and anthropomorphic soft hands [5], [6]. The input pressure is shaped by the enclosed air chamber, and generates deformation-dependent actuation forces that keep perpendicular to the chamber's surface. Hence, the morphological shape of a pneumatic soft robot plays an essential role in programming the motion behavior, not only by shaping the soft-bodied structural characteristics but equally importantly, by locally orienting the actuation forces.

A fundamental open issue is how to inversely design the morphology of a pneumatic soft robot, including the interior air chamber and the exterior profile, for achieving the desired motion behavior. Although design approaches for soft robots have been developed [7], tailored to multimaterial distribution [8]–[10], wrapping fibers [11], reinforced skeleton [12], [13], and external fields for actuation [14], [15], the morphological design of pneumatic soft robots is still in general elusive and nontrivial, mainly due to high dimensionality of the freeform chamber's shape (*amorphousness*) and high dependency of the robot's large deformation on the pressurized chamber's shape through complicated soft material mechanics (*sensitivity*). To date, it is still difficult, if not impossible, to identify the optimum shape of pneumatic channels within the large potential design space. Instead, geometry design of existing pneumatic soft robots is usually determined heuristically, leading to significant time spent on iterating hardware and underperforming robots.

Over the years, prototypes of pneumatic soft actuators and robots have been extensively reported, but the employed air chamber's shape has limited solutions, most of which are intuitive, e.g., bellows for linear motion [16] and pneumatic networks (PneuNets) for bending motion [17]. These heuristic design paradigms, however, cannot directly generate the optimal geometry parameters for various constituent materials and may quickly become less effective when dealing with complex motions. Besides, lacking of deliberate consideration on stiffness, intuitive designs usually suffer from unsatisfactory load capability. To improve the performance in terms of motion range and payload, parametric optimization has been conducted to tailor the shape of bellows [18], PneuNets [19], [20] and vacuumed air chamber [21], but the design exploration was still inevitably limited within the predefined regular shape.

The importance of geometrically exploring the air chamber to permit larger design space has been increasingly recognized, and some successful attempts toward the rational shape design were made [7]. By tailoring the aspect ratio of

This work was supported by the National Natural Science Foundation of China (Grants No 52275026 and 91948302). (*Corresponding author: Feifei Chen*.) (Feifei Chen and Zenan Song contributed equally to this work.)

The authors are with State Key Laboratory of Mechanical System and Vibration, Shanghai Jiao Tong University, and School of Mechanical Engineering, Shanghai Jiao Tong University, Shanghai 200240, China (email: ffchen@sjtu.edu.cn; sssnnn7119@sjtu.edu.cn; stonehot@sjtu.edu.cn; guguoying@sjtu.edu.cn; mexyzhu@sjtu.edu.cn).

Feifei Chen, Guoying Gu, and Xiangyang Zhu are also with Meta Robotics Institute, Shanghai Jiao Tong University, Shanghai 200240, China.

IEEE Transactions on Robotics (T-RO) paper, presented at ICRA 2024, Yokohama, Japan. Cite as T-RO paper.

the rectangular air channel embedded such that deformation along the channel routing direction dominates, Siéfert *et al.* achieved the morphing of a planar rubbery sheet into a predefined three dimensional shape [22]. Instead of relying on air channels of regular shape, Chen *et al.* demonstrated high-performance linear actuators based on triply periodic minimal surface [23] and twisting actuators based on chiral freeform surface [24]. Maloisel *et al.* recently proposed an innovative design strategy of routing one-dimensional curved muscle fibers that are pneumatically actuated in a rubber matrix, and the routing pathway and applied pressure were optimized to achieve the desired deformation [25]. However, the employed muscle fibers required extra fabrication and data-driven characterization, and their inlet and outlet location was non-designable. Researchers have also investigated topology optimization of air chambers to produce bending motion of soft actuators, using density-based methods, but the required gradient information was not analytically derived [26], or was inaccurate due to unrealistic small strain assumption [27].

The initial attempts above are inspiring, but still do not arrive at a general solution to morphological design of pneumatic soft robots. In this article, we consider the general problem of simultaneously designing the interior air chamber's shape and exterior profile of a pneumatic soft robot, as well as the input pressures of the air chambers, to obtain the desired deformation behavior (see Fig. 1). We propose a concurrent shape optimization approach in which the freeform shapes of interest are independently tracked by dynamic B-spline based surfaces, and they co-evolve by gradient-based optimization. The shape derivative, in a unified mathematical form, captures how the morphological features quantitatively modulate the deformation behavior by simultaneously varying the structural and actuation characteristics. The geometric and material nonlinearities are rigorously considered to obtain accurate gradient information that guarantees convergence towards the (local) optimum. Further, to reckon with the robot's load capability, the external loads are incorporated into the design framework as a predefined input, including the ubiquitous gravity which, however, was not considered in most existing model-based design methods [22]–[24], [27], except a few [25].

A major challenge of performing morphological optimization is how to regulate the surface quality. For instance, regions of high curvature typically cause severe difficulty in finite element analysis since the mesh is prone to distortion [28], and bring difficulty in the molding-based fabrication which is widely used for pneumatic soft robots. In this regard, we propose a surface control strategy by imposing a constraint on the principal curvatures. In the meantime, an additional constraint on the minimal distance between surfaces (or within a surface) is applied to avoid unexpected topological change, such as merging of interior and exterior surfaces or self-intersection of a surface. By virtue of the analytical shape representation, these geometric constraints are readily integrated into the morphological optimization framework as penalty functions, with no need of additional post-processing on design during the optimization iterations.

To validate the effectiveness of our proposed design approach, we first showcased applications of actuators that perform basic deformation modes including elongating, bending, and twisting. It is found that, through this approach, effective designs of smooth morphology are automatically produced with high performance in terms of deformation and load capabilities, a trade-off between which can be conveniently tuned by designers in the unified design framework. The simulation and experiments are well in line and indicate that morphological characteristics of the optimized design are physically explainable. Further, we show robot arms that exhibit the predefined in-plane and out-of-plane configurations. Multi-target configurations are also achieved by concurrently optimizing the morphology and the input pressures of multiple chambers, as demonstrated by reconfigurable soft robot arms with various deformation modes. These examples verify the generality of our method to tackle with complex design problems that in contrast may quickly render intuitive designs ineffective.

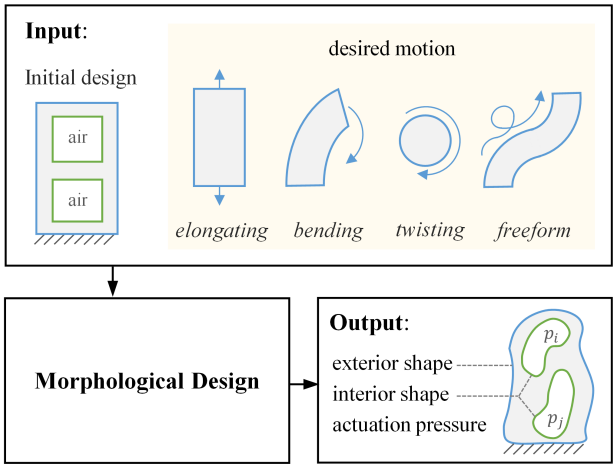

Fig. 1: Morphological design of a pneumatic soft robot for desired motion behavior by automatically determining the exterior and interior shape as well as the input pressures.

The main contributions of the proposed optimization-based design framework include:

1) an automatic inverse design approach that concurrently determines the interior and exterior shape of pneumatic soft robots and the input air pressures;
2) a curvature and distance control strategy integrated in the morphological optimization to guarantee high-quality surface;
3) a sub-optimization based strategy to effectively and efficiently evolve the morphology at a minimal cost on performing finite element analysis.

II. Design Problem Formulation

Our design paradigm for pneumatic soft robots is presented in Fig. 1. The design approach takes as input the desired motion and an initial design, and aims to produce as output the morphology which is fully captured by the interior air chamber's shape and the exterior shape. The morphological design is posed as a continuous optimization problem, where the interior and exterior shapes are optimized, in a concur-

rent and iterative way. The design paradigm has three basic assumptions as follows.

1) The pneumatic soft robot in question is made of a single homogeneous material. That is, we focus on the geometry design of soft robots.
2) We limit the morphological evolution to change in shape only, and assume that the topology, i.e., the number of the air chambers, is predefined and keeps unchanged during the design process.
3) The external payload of interest includes only the gravitational force and concentrated force or moment at fixed regions, e.g., the end-effector.

A. Geometric Model: B-spline Surface

A three dimensional soft body can be uniquely shaped by a set of 2-manifold boundaries, including the interior and exterior surfaces. To allow sufficient geometric flexibility, each surface is independently described by B-spline functions as follows,

$$\mathbf{r}^{\text{in}}(q,r) = \sum_{j=1}^{m^{\text{in}}} \sum_{i=1}^{n^{\text{in}}} \mathbf{P}_{ij}^{\text{in}} B_i^q(q) B_j^r(r) \tag{1}$$

$$\mathbf{r}^{\text{ex}}(q,r) = \sum_{j=1}^{m^{\text{ex}}} \sum_{i=1}^{n^{\text{ex}}} \mathbf{P}_{ij}^{\text{ex}} B_i^q(q) B_j^r(r). \tag{2}$$

where $\mathbf{r} \in \mathbb{R}^3$ represents any point of interest on a undeformed boundary surface, with q, r the direction indices, $\mathbf{P}_{ij} \in \mathbb{R}^3$ denotes the control point with indices of i and j in q and r directions, respectively, B_i^q is the basis function of the i-th control point in q direction. Throughout the article, the superscript $^{\text{in}}$ denotes variables for the interior surface, while the superscript $^{\text{ex}}$ denotes variables for the exterior surface. The shape basis function is a piecewise polynomial function whose high order forms can be derived by the Cox-de Boor recursion formula (see Appendix A).

The interior and exterior shapes are topologically equivalent to a cylindrical shell. The knot vectors of the B-splines are located on a grid spanning the fixed cylindrical domain, with a regular spacing in the longitudinal and latitudinal directions. An example of the interior and exterior shapes is shown in Fig. 2. To obtain a closed cavity for pneumatic actuation, the interior and exterior surfaces can be sealed at the two ends, or one may let the surface boundary at each end collapse into a point. The B-spline basis functions are locally supported, and the support domain can be adjusted by knot manipulations [29], allowing convenient control of surface properties such as local smoothness. For a B-spline surface with order k (order of the polynomial) along the latitudinal direction (indexed by q), wrapping the first and last k control points yields the circumferential closure. The first and last knots along the longitudinal direction (indexed by r) are repeated by $k+1$ times, for the purpose of clamping the surface top and bottom.

B. Mechanical Model

We consider a hyperelastic soft body, and without loss of generality, its strain energy density is described by the generalized Neo-Hookean model. In the context of geometric nonlinearity, we employ the deformation gradient as strain measure and the first Piola-Kirchhoff as stress measure which are work-conjugate. The expression of the strain energy density and the first Piola-Kirchhoff stress is provided in Appendix B.

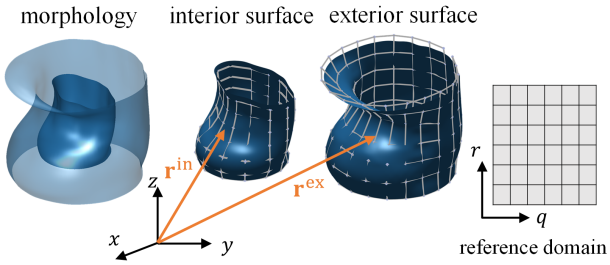

Fig. 2: Morphological shape described by B-splines, including the interior and exterior surfaces.

The state equation can be derived based on principle of energy conservation,

$$\mathcal{A}(\mathbf{u},\mathbf{v}) = \mathcal{B}(\mathbf{u},\mathbf{v}), \quad \forall \mathbf{v} \in U. \tag{3}$$

with $\mathbf{u}$ the displacement field, $\mathbf{v}$ the virtual displacement which is a test vector belonging to the kinematically admissible space U. The variational structural strain energy induced by the virtual displacement is

$$\mathcal{A}(\mathbf{u},\mathbf{v}) = \int_{\Omega^0} \mathbf{s}(\mathbf{u}) : \nabla \mathbf{v} \mathrm{d}\Omega \tag{4}$$

where $\Omega \in \mathbb{R}^3$ denotes the solid domain encompassing the volume between interior and exterior surfaces, $\mathbf{s}$ denotes the first Piola-Kirchhoff stress. The superscripts 0 and 1 denote variables defined on the undeformed and deformed configurations, respectively. The variational external work induced by the virtual displacement is

$$\mathcal{B}(\mathbf{u},\mathbf{v}) = -p \int_{\Gamma_{\text{in}}^1} \mathbf{v} \cdot \mathbf{n} \mathrm{d}\Gamma + \int_{\Omega^1} \rho \mathbf{g} \cdot \mathbf{v} \mathrm{d}\Omega - k_{\text{eff}} \mathbf{u}_{\text{eff}} \mathbf{v}_{\text{eff}} \tag{5}$$

where p denotes the applied pressure, $\Gamma \in \mathbb{R}^2$ is the boundary, ρ the mass density of the material, $\mathbf{g}$ the gravity acceleration (9.81 $\mathrm{m/s^2}$), and the surface normal $\mathbf{n}$ is defined to always point from the solid phase to the void phase. It is noted that only one air chamber is formulated for the sake of conciseness. The subscript eff denotes variables for the end-effector, with k_{eff} the interaction stiffness at the end-effector. The three terms on the right hand side of (5) represent the virtual work done by the actuation pressure, the gravity, and the external forces, respectively. Herein, the effect of the external concentrated force and moment is modeled by a generalized spring of constant k_{eff} for capturing the interacting stiffness. The spring may store energy caused by tension/compression, bending or torsion, and $\mathbf{u}_{\text{eff}}$ and $\mathbf{v}_{\text{eff}}$ denote the corresponding generalized displacements at the end-effector, e.g., the axial stroke, bending angle, or twisting angle, as will be exemplified in Section VIII.

It is preferred to represent the quantities in the undeformed configuration in which the design domain is defined. The

Nanson's formula relates the deformed and undeformed configurations of an oriented area element by

$$\mathbf{n}\mathrm{d}\Gamma^1_{\text{in}} = \mathbf{m}\cdot\mathbf{F}^{-1}J\mathrm{d}\Gamma^0_{\text{in}}. \tag{6}$$

where $\mathbf{m}(\mathbf{r}) \in \mathbb{R}^3$ is the normal of a surface in the undeformed configuration, $\mathbf{F}$ the deformation gradient. The volume elements are related by $\mathrm{d}\Omega^1 = J\mathrm{d}\Omega^0$ with $J = \det(\mathbf{F})$ the volumetric Jacobian. Thus, the variational work (5) can be rewritten in the undeformed configuration by

$$\mathcal{B}(\mathbf{u},\mathbf{v}) = -p\int_{\Gamma^0_{\text{in}}}(\mathbf{F}^{-1}\mathbf{v})^{\mathrm{T}}\mathbf{m}J\mathrm{d}\Gamma + \int_{\Omega^0}\rho\mathbf{g}\cdot\mathbf{v}J\mathrm{d}\Omega - k_{\text{eff}}\mathbf{u}_{\text{eff}}\mathbf{v}_{\text{eff}}. \tag{7}$$

C. Optimization Model

To pose the optimization problem, we introduce $\mathbf{\Phi}$ as the collection of all design variables ($[\mathbf{P},\mathbf{p}]$), with $\mathbf{P}$ the set of all the control points, $\mathbf{p}$ the set of pressures of all the chambers. The design objective is to find an optimal shape of the soft body, approximating the target shape as closely as possible, while the expected payload is included in the mechanical model as an input. The optimization model is formulated by

$$\begin{aligned}\min_{\mathbf{\Phi}} \quad & \mathcal{J} = \int_{\Gamma_{\text{RoI}}} w_{\text{pos}}f_{\text{pos}}(\mathbf{z},\mathbf{z}^*) + w_{\text{ori}}f_{\text{ori}}(\mathbf{R},\mathbf{R}^*)\mathrm{d}\Gamma \\ \text{s. t.} \quad & \mathcal{A}(\mathbf{u},\mathbf{v}) - \mathcal{B}(\mathbf{u},\mathbf{v}) = 0,\ \forall\mathbf{v}\in U.\end{aligned} \tag{8}$$

where $\mathcal{J}$ is a distance metric that measures the difference between the current configuration and the target configuration, evaluated on the region of interest Γ_{RoI}. The distance comes from position mismatch between the current position $\mathbf{z}$ and the target position $\mathbf{z}^*$, denoted by f_{pos}, and also comes from the orientation mismatch between the current orientation $\mathbf{R}$ and the target orientation $\mathbf{R}^*$ of cross sections or the end-effectors, denoted by f_{ori} that measures the geodesic distance on the 3D manifold of the orientation matrices, as follows,

$$f_{\text{pos}}(\mathbf{z},\mathbf{z}^*) = \|\mathbf{z}-\mathbf{z}^*\|_2^2 \tag{9}$$

$$f_{\text{ori}}(\mathbf{R},\mathbf{R}^*) = \|\log\left(\mathbf{R}^{\mathrm{T}}\mathbf{R}^*\right)\|_{\mathrm{F}}^2 \tag{10}$$

with the subscript F the Frobenius norm, and $w_{\text{pos}}, w_{\text{ori}}$ coefficients for tuning the priority by the user. For instance, the motion of a linear actuator is evaluated in terms of the position of its end-effector, while a bending or twisting actuator is evaluated in terms of the orientation. The definition for penalizing shape mismatching is consistent with existing ones [25]. It is also noted that, from either position or orientation aspects, the distance metric is a function of the displacement field. The state equation (3) is enforced as a constraint.

Remark 1. It is often the case that the target shape is not well defined. For example, one may expect a soft finger to bend as much as possible for conformal grasping when subjected to a given load [12]. In such cases, the design objective in (8) degrades to maximization of purely a displacement or rotation along the prescribed direction, which can be readily addressed by the proposed optimization model, as will be exemplified by the actuator design in Section VIII.

III. Shape Sensitivity Analysis

The B-spline based representation of freeform surface guarantees a sufficiently large design space, but in the meantime a large number of control points lead to dimension dilemma in optimization. The information of derivative is of paramount significance for navigating the vast design space. To simulate the morphological evolution, we introduce pseudo time t to track the perturbation process of shape, and investigate how the desired motion behavior as measured in (8) depends on the perturbation, i.e., the so-called shape derivative, based on which the moving velocity of B-splines can be determined. Here, the sensitivity analysis is carried out with the adjoint method. The Lagrangian is formulated by

$$\mathcal{L} = \mathcal{J} + \mathcal{A}(\mathbf{u},\mathbf{w}) - \mathcal{B}(\mathbf{u},\mathbf{w}) \tag{11}$$

where $\mathbf{w}\in U$ denotes the adjoint displacement field to be determined, playing a role of Lagrange multiplier. It is noted that, the design objective and the energy terms in (11) differ in dimension, which can be addressed by dimension normalization and does not affect the numerical implementation.

A. Derivative of $\mathcal{J}$, $\mathcal{A}$, and $\mathcal{B}$

The derivative of the design objective with respect to the pseudo time is

$$\dot{\mathcal{J}} = \int_{\Gamma_{\text{RoI}}}\left(w_{\text{pos}}\frac{\partial f_{\text{pos}}}{\partial\mathbf{u}} + w_{\text{ori}}\frac{\partial f_{\text{ori}}}{\partial\mathbf{u}}\right)\cdot\dot{\mathbf{u}}\,\mathrm{d}\Gamma \tag{12}$$

To determine the shape derivative of the variational strain energy, the use of Lemma 6.1 in [30] with respect to (4) yields

$$\dot{\mathcal{A}}(\mathbf{u},\mathbf{w}) = \int_{\Omega^0}\dot{\mathbf{s}}(\mathbf{u}):\nabla\mathbf{w}\mathrm{d}\Omega + \int_{\Gamma^0_{\text{in}}\cup\Gamma^0_{\text{ex}}}\mathbf{s}(\mathbf{u}):\nabla\mathbf{w}V\mathrm{d}\Gamma \tag{13}$$

where $V(\mathbf{r})\in\mathbb{R}$ denotes the moving velocity along the normal of a surface in the undeformed configuration, ∇ is the gradient operator with respect to the undeformed configuration, with $\dot{\mathbf{w}}$ set to be zero. Since the pressure loading keeps aligned with the surface normal, the perturbation of surface leads to variation in the work done by the actuation pressure. The associated derivative can be obtained based on Lemma 6.3 in [30], and results in a divergence term, i.e., $-p\boldsymbol{\nabla}\cdot\left(J\mathbf{F}^{-1}\mathbf{w}\right)V\mathrm{d}\Gamma$. Therefore, the derivative of the variational work is

$$\begin{aligned}\dot{\mathcal{B}}(\mathbf{u},\mathbf{w}) = & -p\int_{\Gamma^0_{\text{in}}}\big[J(\dot{\mathbf{F}}^{-1}\mathbf{w})^{\mathrm{T}}\mathbf{m} + \dot{J}(\mathbf{F}^{-1}\mathbf{w})^{\mathrm{T}}\mathbf{m} \\ & + \boldsymbol{\nabla}\cdot\left(J\mathbf{F}^{-1}\mathbf{w}\right)V\big]\mathrm{d}\Gamma + \int_{\Gamma^0_{\text{in}}\cup\Gamma^0_{\text{ex}}}J\rho\mathbf{g}\cdot\mathbf{w}V\mathrm{d}\Gamma \\ & + \int_{\Omega^0}\dot{J}\rho\mathbf{g}\cdot\mathbf{w}\mathrm{d}\Omega - k_{\text{eff}}\dot{\mathbf{u}}_{\text{eff}}\mathbf{w}_{\text{eff}} \\ & - \dot{p}\int_{\Gamma^0_{\text{in}}}(\mathbf{F}^{-1}\mathbf{w})^{\mathrm{T}}\mathbf{m}J\mathrm{d}\Gamma.\end{aligned} \tag{14}$$

It is observed from (13) and (14) that, the time derivatives of the variational strain energy and work in part depend directly on the surface movement as denoted by V, and in part depends indirectly on the surface movement through the chain rule with the displacement field being the intermediate variable.

B. Adjoint Method

Since $\dot{\mathbf{u}}$ is unknown, all terms determined by $\dot{\mathbf{u}}$, including $\dot{\mathbf{s}}, \dot{\mathbf{F}}, \dot{J}$, are collected and their sum is set to be zero by selecting a unique $\mathbf{w}$, often referred to as the adjoint displacement, yielding the so-called adjoint equation,

$$\begin{aligned}&\int_{\Gamma_{\text{RoI}}} \left(w_{\text{pos}} \frac{\partial f_{\text{pos}}}{\partial \mathbf{u}} + w_{\text{ori}} \frac{\partial f_{\text{ori}}}{\partial \mathbf{u}} \right) \cdot \dot{\mathbf{u}} \, \mathrm{d}\Gamma + \int_{\Omega_0} \dot{\mathbf{s}}(\mathbf{u}) : \nabla \mathbf{w} \mathrm{d}\Omega \\ &+ p \int_{\Gamma_{\text{in}}^0} \left[J(\dot{\mathbf{F}}^{-1}\mathbf{w})^{\mathrm{T}} + \dot{J}(\mathbf{F}^{-1}\mathbf{w})^{\mathrm{T}} \right] \mathbf{m} \mathrm{d}\Gamma + k_{\text{eff}} \dot{\mathbf{u}}_{\text{eff}} \mathbf{w}_{\text{eff}} \\ &- \int_{\Omega^0} \dot{J} \rho \mathbf{g} \cdot \mathbf{w} \mathrm{d}\Omega = 0.\end{aligned} \tag{15}$$

After the displacement field $\mathbf{u}$ is solved, the adjoint displacement field $\mathbf{w}$ can be calculated.

Remark 2. In the finite element implementation, the adjoint equation (15) numerically translates into a linear finite element equation $\mathbf{K}(\mathbf{u})\mathbf{w} = \mathbf{Q}$, as in typical nonlinear topology optimization problems [31], where $\mathbf{K}(\mathbf{u})$ is the tangent stiffness matrix (in the deformed configuration) reinforced with the interacting spring k_{eff} at the related degree of freedom, and $\mathbf{Q}$ denotes an assembled vector which is nonzero at degrees of freedom of interest (magnitude determined by the position or orientation mismatch) and zero otherwise.

Combining (12)-(15), the derivative of the Lagrangian $\dot{\mathcal{L}}$ is obtained

$$\begin{aligned}\dot{\mathcal{L}} = &\int_{\Gamma_{\text{in}}^0} \left[\mathbf{s}(\mathbf{u}) : \nabla \mathbf{w} + p \boldsymbol{\nabla} \cdot \left(J \mathbf{F}^{-1} \mathbf{w} \right) - J \rho \mathbf{g} \cdot \mathbf{w} \right] V \mathrm{d}\Gamma \\ &+ \int_{\Gamma_{\text{ex}}^0} \left[\mathbf{s}(\mathbf{u}) : \nabla \mathbf{w} - J \rho \mathbf{g} \cdot \mathbf{w} \right] V \mathrm{d}\Gamma \\ &- \dot{p} \int_{\Gamma_{\text{in}}^0} (\mathbf{F}^{-1}\mathbf{w})^{\mathrm{T}} \mathbf{m} J \mathrm{d}\Gamma.\end{aligned} \tag{16}$$

We may infer the physical significance of the terms in (16). The moving velocity V on the interior and exterior surfaces affect both the structural strain energy and the external work done by the gravity, and the moving interior surface plays an additional important role in modulating the work done by the actuation pressure. This sensitivity analysis results shed light on the complicated dependency of the robot's deformation behavior on the morphological shape and the input pressures, allowing further implementation of optimization strategies for achieving the desired motion.

Remark 3. In the numerical process, $\mathbf{u}_{\text{eff}}$ and $\mathbf{w}_{\text{eff}}$ are merged into the associated displacement vectors that are evaluated at the nodal points, and the spring enters into the global stiffness matrix as an enforcing element for finite element analysis. In this way, the interacting loads affect the sensitivity result (16) not only through the displacement field, but equally importantly, through the adjoint displacement.

C. Relating Velocity of Surface to Velocity of Control Points

The surface movement is caused by the movement of control points, and their velocities are related by

$$V = \frac{\dot{\mathbf{r}} \cdot (\mathbf{r}_q \times \mathbf{r}_r)}{\sqrt{EG - F^2}} = \sum_{i,j} \dot{\mathbf{P}}_{ij} \cdot \left[B_i^q B_j^r \frac{(\mathbf{r}_q \times \mathbf{r}_r)}{\sqrt{EG - F^2}} \right]. \tag{17}$$

with $\mathbf{r}_q, \mathbf{r}_r \in \mathbb{R}^3$ the tangential vector in q or r direction, $E, F, G(\mathbf{r}) \in \mathbb{R}$ the first fundamental form of a surface. Substituting (17) into (16), the derivative of the Lagrangian $\dot{\mathcal{L}}$ is rewritten by

$$\dot{\mathcal{L}} = \sum_{m=1}^{S} \sum_{i,j} \dot{\mathbf{P}}_{ij}^m \cdot \int_{\Gamma_m^0} B_i^q B_j^r \frac{(\mathbf{r}_q \times \mathbf{r}_r)}{\sqrt{EG - F^2}} V^* \mathrm{d}\Gamma \tag{18}$$

with m the surface index, S the total number of surfaces, and the term V^* defined for convenience of expression,

$$V^*(\mathbf{r}) = \begin{cases} \mathbf{s}(\mathbf{u}) : \nabla \mathbf{w} + p \boldsymbol{\nabla} \cdot \left(J \mathbf{F}^{-1} \mathbf{w} \right) - J \rho \mathbf{g} \cdot \mathbf{w}, \forall \mathbf{r} \in \Gamma_{\text{in}}^0 \\ \mathbf{s}(\mathbf{u}) : \nabla \mathbf{w} - J \rho \mathbf{g} \cdot \mathbf{w}, \forall \mathbf{r} \in \Gamma_{\text{ex}}^0. \end{cases} \tag{19}$$

For each surface, the area element can be expressed in terms of the first fundamental form,

$$\mathrm{d}\Gamma = \sqrt{EG - F^2} \mathrm{d}q \mathrm{d}r \tag{20}$$

and thus the derivative of the Lagrangian with respect to each control point is

$$\frac{\partial \mathcal{L}}{\partial \mathbf{P}_{ij}} = \int_D B_i^q B_j^r (\mathbf{r}_q \times \mathbf{r}_r) V^* \mathrm{d}q \mathrm{d}r \tag{21}$$

where D is the reference domain of exterior surface or interior surface that the control point $\mathbf{P}_{ij}$ is associated with. The derivative of the Lagrangian with respect to the pressure is

$$\frac{\partial \mathcal{L}}{\partial p} = - \int_{\Gamma_{\text{in}}^0} (\mathbf{F}^{-1}\mathbf{w})^{\mathrm{T}} \mathbf{m} J \mathrm{d}\Gamma. \tag{22}$$

IV. Constraints

In the morphological optimization, the surface quality is a significant concern. The movement of control points may lead the surface to evolve into irregular or even irrational shapes. There are several constraints that the control points have to comply with throughout the optimization process.

A. Constraint of Minimal Distance

To avoid unexpected merging of different surfaces or very thin features with poor manufacturability, the interior and exterior surfaces must comply with a minimal distance constraint. For instance, the interior surface must reside in the exterior surface, while the exterior surface must reside in a predefined domain to constrain the robot size. On a single surface, the distance control should also be applied to avoid self-intersection, as shown in Fig. 3(a). The distance between two points of interest should fulfill the following inequality constraint,

$$g(\mathbf{r}^m, \mathbf{r}^n) = t_{mn}^* - \|\mathbf{r}^m - \mathbf{r}^n\| \leq 0, \forall \mathbf{r}^m \in \Gamma_m, \forall \mathbf{r}^n \in \Gamma_n \tag{23}$$

with m and n the surface indices, and t_{mn}^* the predefined minimal distance between them.

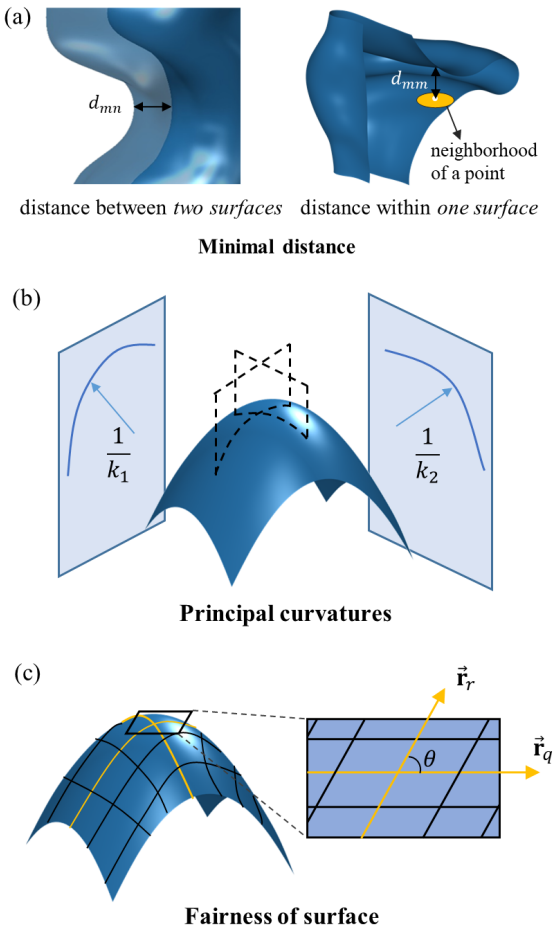

Fig. 3: Constraints: (a) the minimal distance; (b) the principal curvatures; (c) fairness of control points.

Remark 4. For avoiding self-intersecting surfaces, the surface indices are repeated, i.e., $m = n$, and a neighborhood of each point is excluded from calculating the potential energy. The initial radius of neighborhood defined in q and r region is denoted by r^*_{mm}. Self-intersection within the neighborhood can be avoided by restricting the surface curvature as will be described in the following subsection.

The derivative of the constraint function defined in (23) with respect to the control points is,

$$\frac{\partial g}{\partial \mathbf{P}_{ij}} = -\frac{B_i^q B_j^r (\mathbf{r}^m - \mathbf{r}^n)}{\|\mathbf{r}^m - \mathbf{r}^n\|} \tag{24}$$

for $\mathbf{P}_{ij}$ associated with surface m.

B. Constraint of Curvature

Sharp features may induce stress concentration and lead to material failures. Regions of high curvature may cause severe difficulty in finite element analysis since the mesh is prone to distortion [28], and possibly difficulty in the molding-based fabrication which is widely used for pneumatic soft robots. To address this issue, we regulate the surface by constraining the maximal curvature. A penalty function is defined in terms of the principal curvatures,

$$h_1(q,r) = \frac{1}{2}(k_1^2 + k_2^2) = 2H(q,r)^2 - K(q,r) \tag{25}$$

with k_1 and k_2 the principal curvatures, $H(\mathbf{r}) \in \mathbb{R}$ the mean curvature of a surface and $K(\mathbf{r}) \in \mathbb{R}$ the gaussian curvature of a surface.

The derivative of the penalty function with respect to the control points is,

$$\frac{\partial h_1}{\partial \mathbf{P}_{ij}} = 4H\frac{\partial H}{\partial \mathbf{P}_{ij}} - \frac{\partial K}{\partial \mathbf{P}_{ij}}. \tag{26}$$

With the quantities defined in Appendix C, it is straightforward to calculate the derivative.

C. Fairness of Surface

The geometric representation ability of control points may become limited when the surface evolves into irregular shapes. More specifically, it is observed that the surface grows ill-meshed when the angle between the two tangential vectors vanishes or when the magnitude gradient of the tangential vector becomes large. Researchers proposed methods for fairing the surfaces by controlling the length of the tangential vector and its gradient [32]–[34]. Here, we employ a combined surface fairing strategy by constraining both the angle between two tangential vectors and the gradient of their lengths.

The first function is to penalize the deviation of the angle between the two tangential vectors from 90°, defined by

$$h_2(q,r) = \cos^2(\theta) = \frac{F(q,r)^2}{E(q,r)G(q,r)}. \tag{27}$$

The derivative yields,

$$\frac{\partial h_2}{\partial \mathbf{P}_{ij}} = \frac{2F}{EG}\frac{\partial F}{\partial \mathbf{P}_{ij}} - \frac{F^2}{E^2G}\frac{\partial E}{\partial \mathbf{P}_{ij}} - \frac{F^2}{EG^2}\frac{\partial G}{\partial \mathbf{P}_{ij}}. \tag{28}$$

The second term penalizes the gradient of the length of the tangential vectors such that the control points tend to be evenly distributed,

$$\begin{aligned} h_3(q,r) &= \left(\frac{\nabla(\sqrt{E(q,r)})}{\tau_q\sqrt{E(q,r)}}\right)^2 + \left(\frac{\nabla(\sqrt{G(q,r)})}{\tau_r\sqrt{G(q,r)}}\right)^2 \\ &= \frac{E_q(q,r)^2 + E_r(q,r)^2 + 2E_q(q,r)E_r(q,r)}{4\tau_q^2 E(q,r)^2} \\ &+ \frac{G_q(q,r)^2 + G_r(q,r)^2 + 2G_q(q,r)G_r(q,r)}{4\tau_r^2 G(q,r)^2} \end{aligned} \tag{29}$$

where τ_q, τ_r represent the initial dimension of the surface in q and r directions, respectively, for normalization. The derivative of h_3 with respect to the control points is,

$$\begin{aligned} \frac{\partial h_3}{\partial \mathbf{P}_{ij}} =& \frac{E_q + E_r}{2\tau_q^2 E^2}\left(\frac{\partial E_q}{\partial \mathbf{P}_{ij}} + \frac{\partial E_r}{\partial \mathbf{P}_{ij}}\right) \\ &- \frac{(E_q^2 + E_r^2 + 2E_qE_r)}{2\tau_q^2 E^3}\frac{\partial E}{\partial \mathbf{P}_{ij}} \\ &+ \frac{G_q + G_r}{2\tau_r^2 G^2}\left(\frac{\partial G_q}{\partial \mathbf{P}_{ij}} + \frac{\partial G_r}{\partial \mathbf{P}_{ij}}\right) \\ &- \frac{(G_q^2 + G_r^2 + 2G_qG_r)}{2\tau_r^2 G^3}\frac{\partial G}{\partial \mathbf{P}_{ij}}. \end{aligned} \tag{30}$$

The related terms are lengthy in expression but easy to calculate numerically, based on the analytical forms detailed in Appendix C and Appendix D.

Remark 5. The constraints discussed above are purely geometric terms, independent of the displacement field. Thus, the derivative of these constraints can be evaluated directly.

V. Sub-Optimization Problem

Considering the FEA is time-consuming, the trust region method is employed to avoid frequently conducting FEA, by constructing a proxy function that is easy to calculate within a prescribed trust region to approximate the computationally intensive displacement fields. The trust region should be given small enough to ensure accuracy. As long as the optimization converges within this region, one needs to perform FEA and reconstruct the proxy function. In this way, the optimization problem translates into a series of sub-optimization problems.

A. Proxy Function of Objective Function

The change in $\mathbf{\Phi}$ during the current optimization iteration step is denoted by $\mathbf{\Psi} = \mathbf{\Phi}^{k+1} - \mathbf{\Phi}^k$. The sub-optimization problem aims to find a proper $\mathbf{\Psi}$ to update $\mathbf{\Phi}^k$. A proxy Lagrange function $\mathcal{L}^*$ is defined in the sub-optimization problem by the first-order Taylor expansion of $\mathcal{L}$,

$$\mathcal{L}^* = \frac{\partial \mathcal{L}}{\partial \mathbf{\Phi}}^k \cdot \mathbf{\Psi}. \tag{31}$$

B. Penalty Function of Constraints

Meanwhile, the constraints, being highly nonlinear but computationally efficient, remain unaffected and maintain their original formulations. By introducing penalty function, the constrained optimization problem can be transformed into an unconstrained optimization problem. We define the penalty function as

$$f(x) = \begin{cases} 0, & x \le 0 \\ x^b, & x > 0 \end{cases}, \tag{32}$$

which is a b-power function when $x > 0$, which will ensure $(b-1)$-th derivative continuity. Typically, b is assigned a relatively high value, which causes the function to approach zero as $x < 1$ and rapidly increase when $x \ge 1$. In this article, we set $b = 5$.

C. Sub-Optimization Formulation

The unconstrained sub-optimization problem is formulated by

$$\begin{aligned} \min_{\mathbf{\Psi}} \quad & \tilde{\mathcal{L}}^k = \mathcal{L}^* \\ & + \sum_{1 \le m,n \le S} \int_{D_m} \int_{D_n} f\left[\frac{g\left(\mathbf{\Phi}^k + \mathbf{\Psi}\right)}{\epsilon_t}\right] \mathrm{d}q_m \mathrm{d}r_m \mathrm{d}q_n \mathrm{d}r_n \\ & + \int_{\cup_{i=1}^{S} D_i} \sum_{j=1}^{3} f\left[\frac{h_j\left(\mathbf{\Phi}^k + \mathbf{\Psi}\right)}{h_{j\max}}\right] \mathrm{d}q \mathrm{d}r \\ & + f\left(\frac{\mathbf{\Psi} - \mathbf{\Xi}^k}{\epsilon_t}\right) \end{aligned} \tag{33}$$

where $\mathbf{\Xi}^k$ denotes the maximal size of the trust region of design variables, $h_{j\max}$(for $j = 1, 2, 3$) stands for the maximum allowable constraint, and ϵ_t (set to 0.05 mm) denotes the tolerance for the distance penalty.

By combining the derivatives of the Lagrangian (21) and penalty terms (24) (26) (28) (30), it is straightforward to obtain the derivative of $\tilde{\mathcal{L}}^k$ in (33) with respect to $\mathbf{\Psi}$. Since the analytical form is rather lengthy, here we briefly show that it is function of the basic geometric terms which can be readily computed numerically,

$$\frac{\partial \tilde{\mathcal{L}}^k}{\partial \mathbf{\Psi}} = \tilde{\mathbf{L}}'(\mathbf{u}, \mathbf{w}, B_i^q, B_j^r, B_i^{q'}, B_j^{r'}, B_i^{q''}, B_j^{r''}). \tag{34}$$

D. Optimization Method

To solve the sub-optimization problem which is highly non-convex, we first utilize the quasi-Newton method to determine the optimization direction, and then employ a backtracking line search to determine the step length.

The sub-optimization problem is iteratively solved by

$$\mathbf{\Psi}^{l+1} = \mathbf{\Psi}^l - \alpha_l B_l^{-1} \nabla \tilde{\mathcal{L}}^k, \tag{35}$$

where α_l is the step size by the backtracking line search method, B_l is a symmetric positive definite matrix determined by the Davidon-Fletcher-Powel (DFP) method as the estimation of the Hessian matrix of $\tilde{\mathcal{L}}$,

$$B_{l+1}^{-1} = B_l^{-1} + \frac{s_l s_l^{\mathrm{T}}}{y_l^{\mathrm{T}} s_l} - \frac{B_l^{-1} y_l y_l^{\mathrm{T}} B_l^{-1}}{y_l^{\mathrm{T}} B_l^{-1} y_l}, \tag{36}$$

with $s_l = \mathbf{\Psi}^{l+1} - \mathbf{\Psi}^l$, and $y_l = \nabla \tilde{\mathcal{L}}^{k,l+1} - \nabla \tilde{\mathcal{L}}^{k,l}$ the change in the gradient of the objective function.

E. Convergence Criteria

Due to the large number of variables involved in the highly non-convex sub-optimization problem, convergence can be challenging to achieve. Therefore, two convergence criteria are used, and the optimization will be terminated if either of them is met. The first criterion is that the step size searched by line search satisfy $\alpha_k < \epsilon_\alpha$, typically with $\epsilon_\alpha = 10^{-5}$. The second criterion is that the number of iterations reaches a maximum limit, denoted by $l > \aleph^k$. By controlling the value of $\aleph^k$, one can tailor the frequency of performing FEA and sensitivity analysis for obtaining a more accurate proxy function. We propose a strategy as follows,

$$\aleph^{k+1} = \begin{cases} \beta_1 \aleph^k, \lambda \le 0.2 \\ \beta_2 \aleph^k, \lambda > 0.2 \end{cases}, \tag{37}$$

where λ is the criterion, defined as

$$\lambda = \frac{\left\| \frac{\partial \tilde{\mathcal{L}}}{\partial \mathbf{\Phi}}^{k+1} - \frac{\partial \tilde{\mathcal{L}}}{\partial \mathbf{\Phi}}^{k} \right\|_1}{\left\| \frac{\partial \tilde{\mathcal{L}}}{\partial \mathbf{\Phi}}^{k} \right\|_1}. \tag{38}$$

In this work, we set $\beta_1 = 1.2$, $\beta_2 = 0.9$. The idea behind is, when the gradient changes rapidly, one tends to reduce the sub-optimization iterations and more frequently perform FEA, and vice versa, to achieve an accuracy-speed tradeoff for ensuring a stable reduction of the objective function in either case.

Algorithm 1: Design Optimization Workflow.

while *not converged* **do**
  Geometric Modelling :
  Create interior and exterior surfaces in Matlab as B-spline surfaces;
  Export control points to Rhino and surface information to Abaqus;
  Enclose the surfaces to create the 3D entity in Rhino;
  Export the 3D entity (.igs file) as input for Abaqus;
  Finite Element Analysis:
  Assign the entity with the generalized Neo-Hookean material model;
  Define surface sets based on imported information from Matlab for preprocessing;
  Apply pressure loads and boundary conditions to the defined surface sets;
  Mesh the solid part with `C3D10H` element;
  Submit the job;
  Extract the coordinates and connection of nodes, displacement, and adjoint displacement;
  Solve the adjoint equation (15);
  Sensitivity Analysis :
  For a surface of interest, identify all tetrahedral elements that have at least three nodes on the surface, denoted by set $\mathcal{T}$;
  Evaluate the velocity term (19) at the center points of all elements in set $\mathcal{T}$ (see Appendix E);
  Evaluate the velocity term (19) at the surface's points mapped from the nodes in regular $q-r$ domain by the nearest-neighbor interpolation;
  Calculate the derivative of all design variables using (21) and (22);
  Sub-Optimization :
  Formulate the sub-optimization problem (33);
  while *sub-optimization not converged* **do**
    Find the quasi-Newton direction using the DFP algorithm in (36);
    Find the step size α_l using the backtracking line search algorithm;
    Update $\boldsymbol{\Psi}$;
  end
  Update $\boldsymbol{\Phi}^{k+1} = \boldsymbol{\Phi}^k + \boldsymbol{\Psi}$;
end
Save and visualize the optimization result.

VI. Numerical Workflow

In the design workflow, the interior and exterior shapes are iteratively renewed by the optimization procedure, as shown in Algorithm 1 and Fig. 4. The whole workflow mainly includes four parts: geometry modelling, finite element analysis, sensitivity analysis, and solving the sub-optimization problem.

The B-spline surfaces are initialized such that the angle between q and r directions is 90° and the control points are evenly distributed in the two directions. In order to facilitate the occurrence and evolution of potential geometric features, small sinusoidal perturbations may be applied in both directions for increasing the convergence rate. The analytical geometric model is firstly built in the commercial software Matlab. Subsequently, the control points data are exported into Rhino to generate the surfaces as defined by B-splines, followed by a trimming operation for enclosing the surfaces.

For the nonlinear finite element analysis compatible with varying shape, we customize an automatic numerical framework by connecting Matlab, Rhino and Abaqus. We adopt `C3D10H` elements (10-node quadratic tetrahedron and hybrid) for the soft rubber. Herein, the order of element should be at least quadratic to permit computing the divergence term in surface velocity (19) that involves the second-order derivative of the interpolation function, as detailed in Appendix E.

The optimization starts from an initial regular design, e.g., a cylindrical shape combined with small sinusoidal perturbations, followed by nonlinear finite element analysis to evaluate the deformation behavior of the actuator. The adjoint displacement is solved by (15). The velocity of a surface of interest is firstly evaluated at the center points of all the tetrahedral elements which have at least three nodes on the surface. The detailed computation is introduced in Appendix E. To avoid the complicated inverse mapping from the curved surface to the $q-r$ domain, we initially create a structured mesh within the $q-r$ domain and map it onto the surface. Subsequently, we interpolate the surface's velocity on the mapped points using the nearest-neighbor interpolation method, for calculating the derivative based on (21). Thereafter, the sub-optimization problem is constructed and solved by the quasi-Newton method and the backtracking line search strategy. The above process is repeated until the design candidate fulfills the predefined convergence criterion. That is, the maximal change of the design objective is smaller than a predefined threshold value. It is noted that, although the finite element mesh varies with the evolved surface, the sensitivity can be well approximated as long as the mesh quality is fine, and the remeshing operation can hardly affect the stable evolution of surface. Table I lists the related parameters in the numerical implementation.

VII. Material and Fabrication

Since the pneumatic actuator sustains large deformation upon pressurization, the stretchability and endurance must be considered during the selection of fabrication method and materials. We use Hei-Cast 8400 (Wenext, China) with the hardness of shore 40 A, whose shear modulus is $0.49\,\mathrm{MPa}$ and bulk modulus is $4.80\,\mathrm{MPa}$ fitted from mechanical tests.

The optimized soft robots are expected to have complex geometry with distributed negative draft angles. To ensure the fabrication precision and alleviate the difficulty of material forming, we adopt the compound molding method, which is realized by the following steps. First, a rigid actuator prototype that may contain several parts is fabricated through 3D printing using hard epoxy. Second, the rigid prototype is dipped in liquid silicone rubber to obtain a soft negative mold of the actuator. Third, the soft rubber (Hei-Cast 8400, 40A) is injected into the mold to obtain the soft counterparts of the

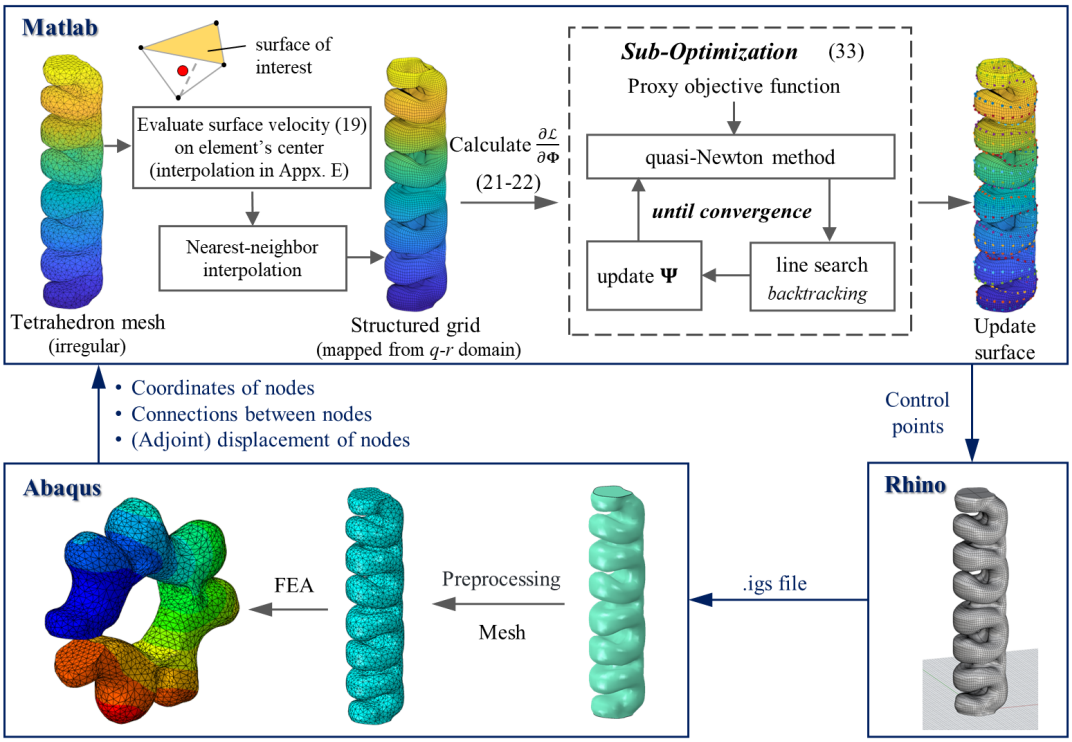

Fig. 4: Numerical implementation of design optimization.

TABLE I: Parameters

Parameter	Value
Shear modulus of rubber μ (MPa)	0.49
Bulk modulus of rubber κ (MPa)	4.80
Mass density of rubber ρ (g/cm^3)	1.10
Minimal distance between different surface t^*_{mn} (mm)	2
Minimal distance within one surface t^*_{mm} (mm)	1
Radius of neighborhood within one surface r^*_{mm} (mm)	2
Initial density of control points (mm^{-1})	0.6
Initial maximum number of iteration of sub-optimization $\aleph^1$	200
Order of barrier function b	5
Maximum step size Ξ^k (mm)	0.2
Maximum allowable constraint $h_{1\max}$	0.3
Maximum allowable constraint $h_{2\max}$	0.2
Maximum allowable constraint $h_{3\max}$	0.1
Tolerance for the distance penalty ϵ_t (mm)	0.05
Order of the B-spline surface	3
Order of the target B-spline curve in shape matching	3

divided actuator. Finally, the soft pieces are glued together to form an integral part.

It is noted, however, the bonding operation with glue usually leads to unexpected stiffness reinforcement to some extent, which may weaken the deformability and load capacity of the robot. Besides, the soft negative mold typically experiences an unavoidable deformation under the gravity effect, which to some extent limits the manufacturing precision. This effect contributes in part to the error between the experiment result and the theoretical prediction in Section VIII.

VIII. Results

In this section, we showcase four applications to validate our method, including design of actuators for basic extension, bending, and twisting motions, and continuous robot arms that perform the desired spatial configuration in which the gravity is particularly considered at the design stage.

A. Linear Actuator

Linear motion is the most basic mode of actuation for soft robots, and multiple linear motions in space can work in concert to produce complex motion behaviors [35], in an analog to humans' muscle fibers. Here, we investigate the inverse morphological design of a soft linear actuator that is expected to elongate as largely as possible when pressurized. It is fixed at one end and interacts with the external environment at the other end, as shown in Fig. 5(a). The interacting stiffness is represented by a linear spring along the axial direction which is attached to the center of the end-effector. The design domain is a cylinder within which the interior and exterior surfaces are optimized, while the two ends each are enforced to experience in-plane shape variation only.

The interior and exterior surfaces are initially cylindrical with their size shown in Fig. 5(a). The control points are iteratively renewed through repeated sub-optimization processes and lead the surfaces to evolve into freeform geometry. Since the two end surfaces each are capped with a rigid plate, the control points on either the top or bottom layer are supposed to

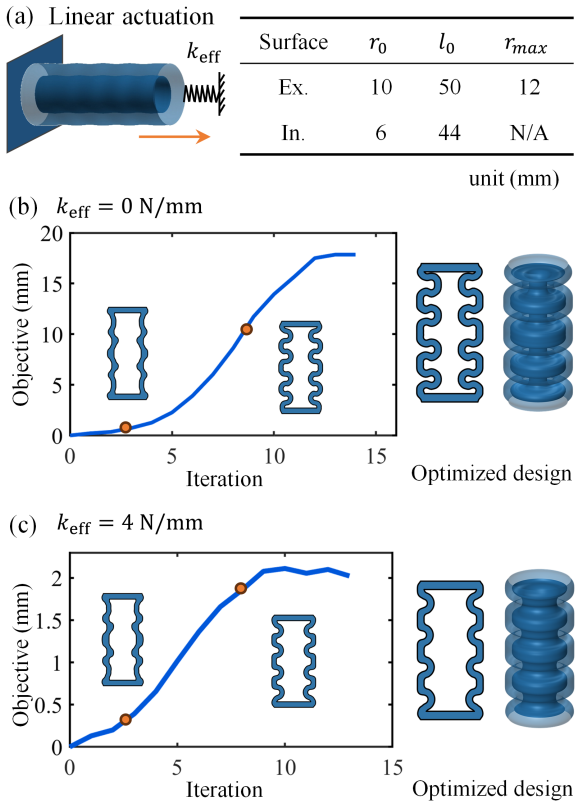

Fig. 5: Linear actuator design: (a) the schematic of the actuator and geometric parameters; the optimization history and results for different interaction stiffness (b) $k_{\text{eff}} = 0$ and (c) $k_{\text{eff}} = 4\,\text{N/mm}$.

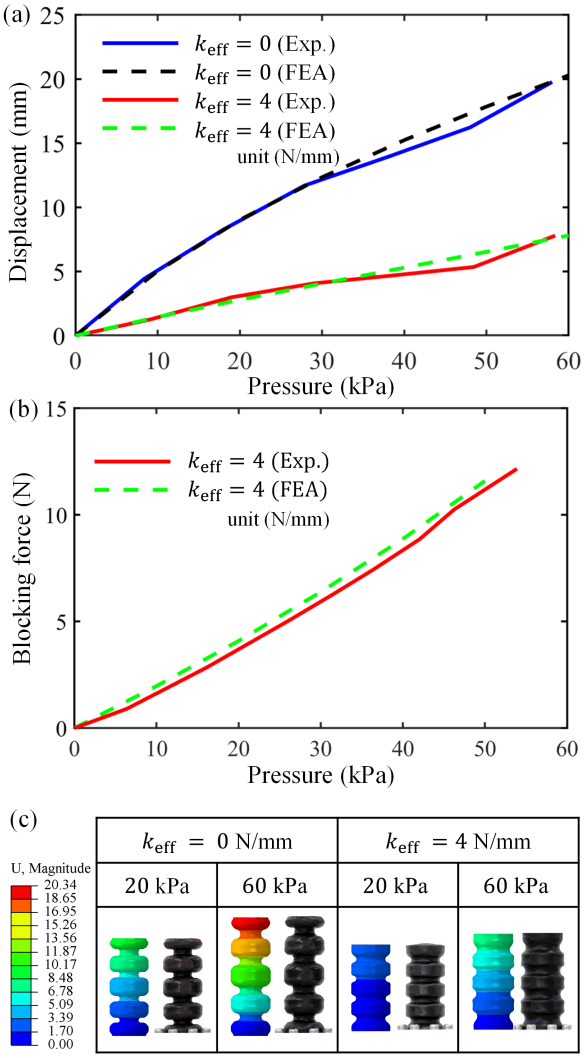

Fig. 6: Experiment results of the linear actuator: (a) the relationship between the axial displacement and the actuation pressure; (b) the relationship between the blocking force and the actuation pressure; (c) the deformed configurations of the investigated designs at different levels of pressure.

be on a plane during optimization, and their moving velocity along the plane's normal are lumped to generate a "rigid body" motion. The history of the design objective, i.e., the axial displacement of the end-effector, is shown in Fig. 5(b). Also plotted are the intermediate designs during the optimization. By controlling the minimal distance between the interior and exterior surfaces, the minimum thickness of rubber can be restricted. By controlling the minimal distance between one surface and itself, the self-intersection can be avoided. The complete morphological optimization process is provided in Movie S1.

The optimized design is characterized by periodic bellows, which are similar to existing linear actuators [16]. It has been well understood that the bellows weaken the stiffness along the axial direction and thus the axial elongation dominates upon pressurization. It should be noted that, even for this simple design task, our model-predictive optimization is still advantageous by simultaneously generating the optimal geometric features and their size, in an automatic manner, which saves the computational cost of brute-force search of optimal parameters based on an empirical design [18].

It is specially investigated how the optimal morphology depends on the external interaction, by tailoring the spring stiffness. Herein, we compare the optimized results with $k_{\text{eff}} = 0$ and $k_{\text{eff}} = 4\,\text{N/mm}$, as shown in Figs. 5(b) and (c) respectively. It is observed that the former presents more deeply folded features that expand remarkably upon pressurization in the axial direction, while the latter is characterized with less deep folds and larger cross section on average to attain better load capability for interaction. It is more comprehensively shown in Movie S1 how the optimized design varies with the predefined interacting stiffness, and the geometric features experience a continuous transition. The general trend is, with the increase of the interaction stiffness, the optimization solution trades compliance for stiffness.

To validate the effectiveness of the optimized design, we further carry out experiments including the free motion and blocking force tests. Fig. 6(a) shows the free travel trajectory of the optimized linear actuator. The actuator prototype is pressurized at a speed of $5\,\text{kPa/s}$ to simulate a quasi-static process. The free motion exhibits excellent repeatability. For both designs with $k_{\text{eff}} = 0$ and $k_{\text{eff}} = 4\,\text{N/mm}$, the axial elongation increases with the applied pressure monotonously.

The result of nonlinear finite element analyses matches well with the experiment trajectories in the range of 0-60 kPa with the maximal deviation less than 5.0%.

The blocking force reflects the load capability of the actuator. For the design without specification on interaction stiffness, the actuator may easily buckle when blocked, indicating low stiffness. For the design with $k_{\text{eff}} = 4\,\text{N/mm}$, the blocking force increases with the applied pressure, peaking at $12.15\,\text{N}$ under $54\,\text{kPa}$, as shown in Fig. 6(b). It is observed that the blocking force as measured is smaller than the simulation prediction. The error may be in part due to the misalignment between the force sensor and the actuator, and in part due to the manufacturing error.

B. Bending Actuator

The second case deals with bending motions that play a central role in soft grasping [5] and multi-legged locomotion [36]. Bending is closely related to linear motions since it is caused by asymmetry in tension or compression. As indicated by the widely used PneuNets design [17] for soft bending actuators, the featured multiple air chambers at the tensile side are geometrically similar to half of bellows. Along the compressive side is usually placed a piece of solid or unstretchable material as the so-called strain limiting layer. The challenge for design is to tailor the stiffness of the tensile and compressive sides such that there is sufficient asymmetry in stiffness for bending and in the meantime the overall stiffness can well interact with external loads.

In this case, the design objective is to maximize the bending angle when the actuator is pressurized and loaded, as indicated by Fig. 7(a). Herein, purely in-plane bending is investigated, and thus the actuator is symmetric. During optimization, the tensile and compressive sides exhibit apparently different features, and as expected, the optimization results for different interaction stiffness are obviously different.

When there is no specification for interaction, i.e., $k_{\text{eff}} = 0$, the optimized design exhibits periodic wave-like features on the tensile side and flat features on the compressive side, similarly to the PneuNets design [17]. The optimization process witnesses increasingly pronounced waves and the resulting valley regions grow thinner which play a role as flexure hinges for generating bending motions as much as possible.

When there is requirement for interaction stiffness, e.g., represented by an arc spring $k_{\text{eff}} = 100\,\text{N} \cdot \text{mm/rad}$, the optimized design presents different features. Although periodic waves also appear, the whole morphology becomes more integral as evidenced by the interconnection between adjacent air chambers through rib-like features on the lateral surface. The complete optimization process is provided in Movie S2. Fig. 8 further shows how the actuator's morphology transits with the increase of the interaction stiffness, from which merging between air chambers can be observed. In this way, the cross-sectional area of the actuator increases, eliminating the compliant hinges, which endows the actuator with higher stiffness to withstand the in-plane loads. To the best knowledge of the authors, the structural features for interaction stiffness, i.e., the rib-like channels connecting the neighboring air chambers, have not been reported in existing soft bending actuators.

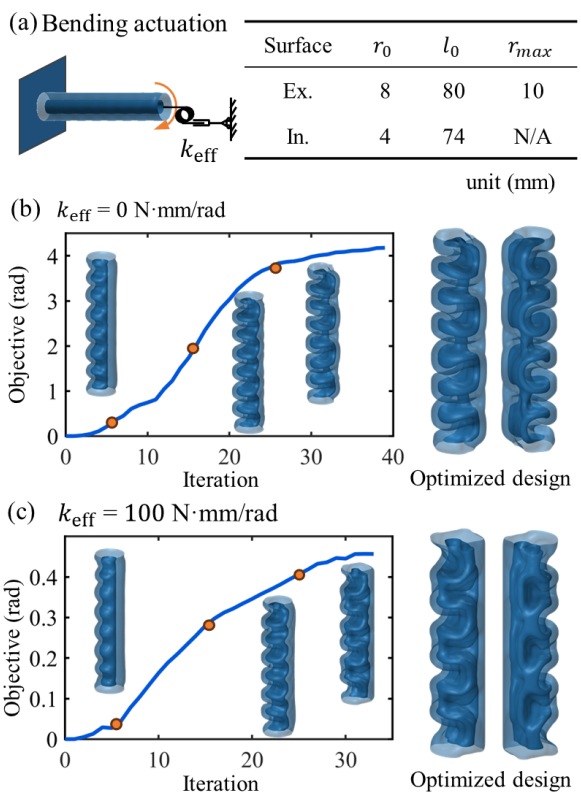

Fig. 7: Bending actuator design: (a) the schematic of the actuator and geometric parameters; the optimization history and results for different interaction stiffness (b) $k_{\text{eff}} = 0$ and (c) $k_{\text{eff}} = 100\,\text{N} \cdot \text{mm/rad}$.

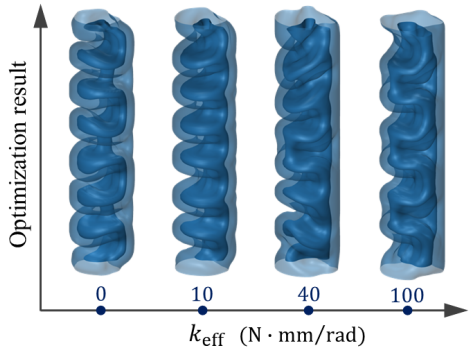

Fig. 8: The optimized results for different interaction stiffness.

Fig. 9 shows the experiment results of the bending actuator. Both the free bending angle and the blocking force increases monotonously with the applied pressure, and the simulation predictions are well in line with the experiment results even at large deformation. It is noted that, although the design with $k_{\text{eff}} = 0$ has remarkably large bending motion, its low stiffness leads to quite low blocking force which would limit its use in practical scenarios such as grasping tasks. On the contrary, the design with $k_{\text{eff}} = 100\,\text{N} \cdot \text{mm/rad}$ attains more balanced performance in terms of the bending angle ($> 100°$) and blocking force ($>1.1\,\text{N}$).

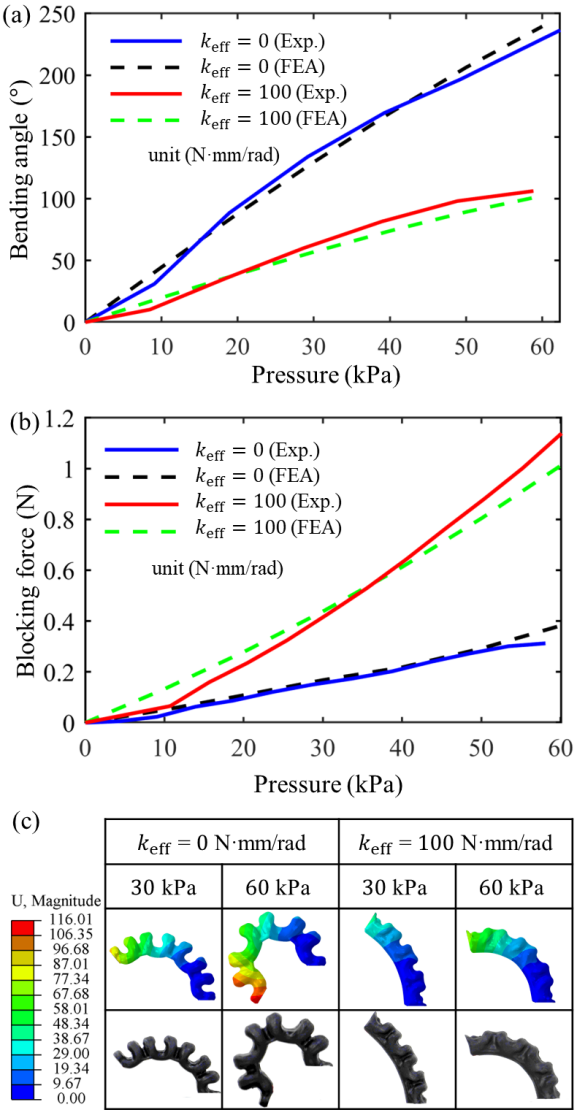

Fig. 9: Experiment results of the bending actuator: (a) the relationship between the bending angle and the actuation pressure; (b) the relationship between the blocking force and the actuation pressure; (c) the deformed configurations of the investigated designs at different levels of pressure.

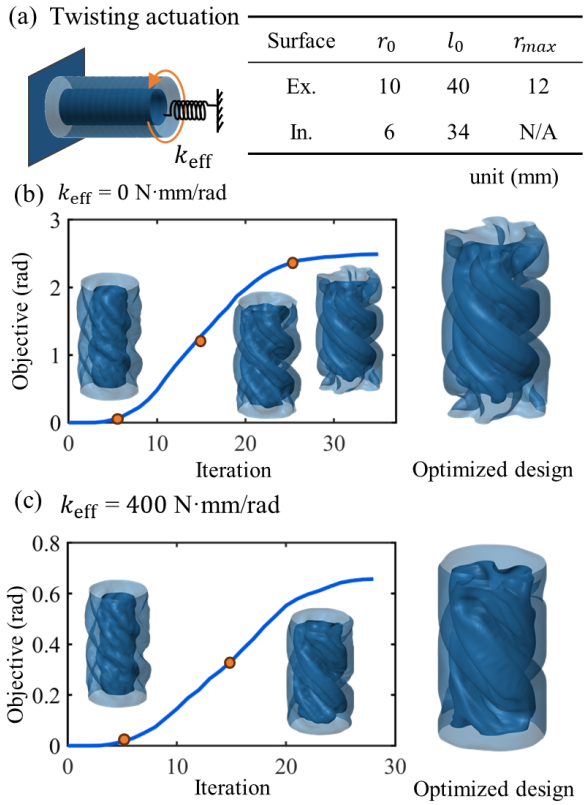

Fig. 10: Twisting actuator design: (a) the schematic of the actuator and geometric parameters; the optimization history and results for different interaction stiffness (b) $k_{\text{eff}} = 0$ and (c) $k_{\text{eff}} = 400\,\text{N}\cdot\text{mm/rad}$.

C. Twisting Actuator

Twisting is also an important mode of motion in soft robots for grasping and locomotion applications [37], [38]. Compared with linear and bending motions, twisting is less intuitive or understood. It is commonly recognized that oblique features are supposed to be included for generating a twist. In this case, the actuator connected to a coil spring is expected to twist as largely as possible upon pressurization, as shown in Fig. 10(a). We made an assumption that each cross section has 3-fold rotational symmetry (120°). Besides, since the two parts of the actuator contribute equally to the twisting motion, the interior and exterior shapes themselves are central symmetric about the center of the middle plane.

The evolution of design starts from a cylindrical shape. During the optimization process, it is observed that spiral air channels grow, referring to the intermediate designs in Fig. 10(b). The complete optimization process is provided in Movie S3. It is specially noted that, owing to the surface fairing (27) and (29), although the features undergo rather large changes, the B-spline surface can still well capture the geometry during optimization.

It is also investigated how the interaction stiffness affects the optimization solution. When there is no interaction specification, i.e., $k_{\text{eff}} = 0$, the air chamber becomes increasingly thinner in the early optimization process for reducing the stiffness to produce larger twisting motion, until reaching the minimal distance limit. Subsequently, the thickness remains almost constant, and the spiral features grow pronounced, leading to a phase difference of almost 360° between the top and bottom plates, which is consistent with the pre-twisting design in existing works [24], [37].

When there is requirement of interaction stiffness, e.g., $k_{\text{eff}} = 400\,\text{N}\cdot\text{mm/rad}$, the optimization solution has similar spiral features. However, the spiral angle is much smaller, and the thickness of each spiral increases until reaching the maximal boundary radius, which helps to obtain a proper torsional rigidity to interact with the coil spring.

The performance of the twisting actuators is experimentally evaluated. The blocking torque is measured by a torque sensor with range $1\,\text{N}\cdot\text{m}$ and resolution 0.05% (DYJN-104, DaYang Sensing, China). The design with $k_{\text{eff}} = 0$ results in an twisting

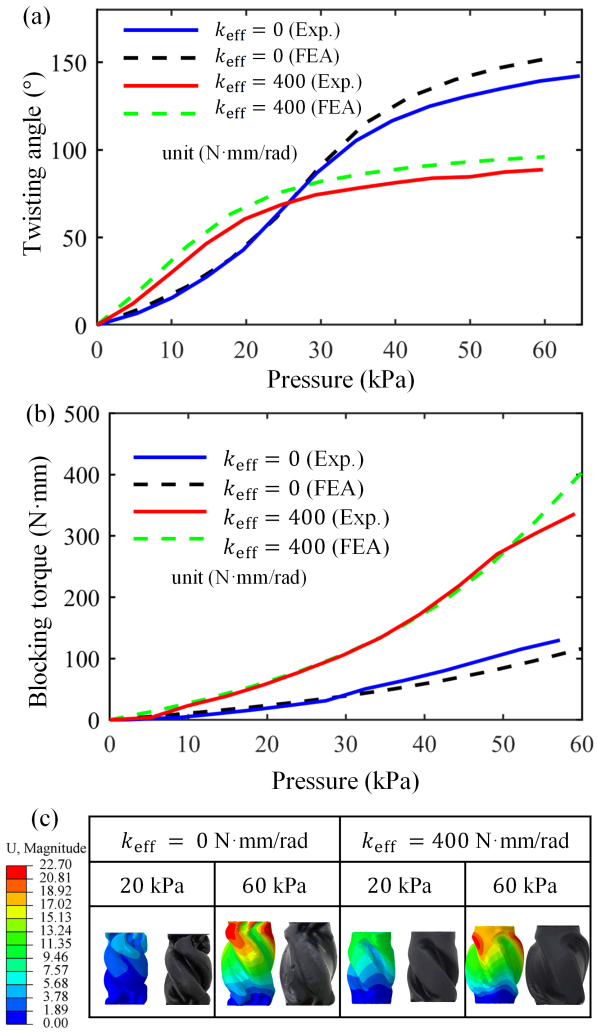

Fig. 11: Experiment results of the twisting actuator: (a) the relationship between the twisting angle and the actuation pressure; (b) the relationship between the blocking torque and the actuation pressure; (c) the deformed configurations of the investigated designs at different levels of pressure.

angle over 140° at 60 kPa and blocking torque of 130 N · mm at 57 kPa, while the design with $k_{\text{eff}} = 400\,\text{N} \cdot \text{mm/rad}$ results in a twisting angle of 85° at 50 kPa and blocking torque of 336 N · mm at 60 kPa, as shown in Fig. 11.

D. Effect of Initial Design

An essential limitation for gradient-based optimization paradigms is that the solution depends on the initial guess, which is generally true for non-convex problems. Besides, the dependency should be considered on a case-by-case basis. We investigate the role of the initial design in the three actuator design problems above, by varying the initial design from perfect hollow cylinders to cylinders perturbated with sinusoidal waves of different periods (the amplitude is fixed to be 0.2 mm). Fig. 12 shows the initial designs and the resulting optimized designs, with the first column being those adopted in Section VIII-A, B, and C. It is found that, a different initial design typically leads to a different optimization result.

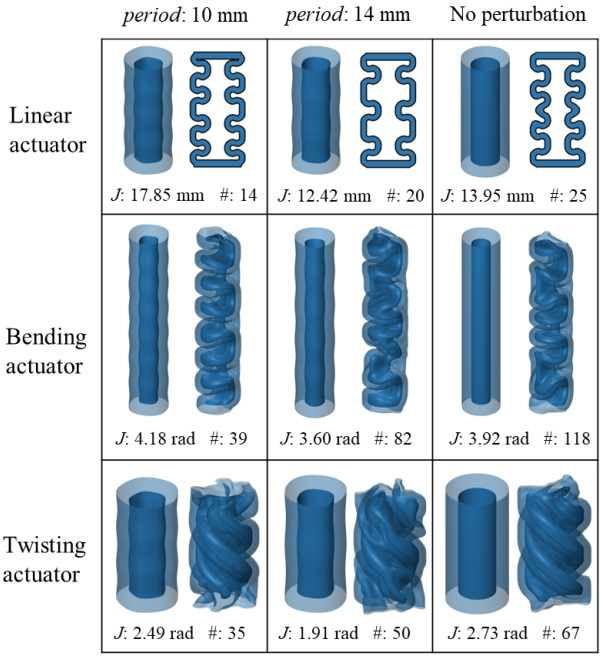

J denotes the actuator performance, # denotes the total iteration number
period denotes the period of sinusoidal perturbation in the initial design

Fig. 12: Effect of the initial design. In each grid, the left is the initial design and the right is the optimization result. J: the actuator performance, #: the total iteration number, *period*: the period of sinusoidal perturbation in the initial design.

Specifically, for the linear and bending actuators, the geometric complexity of the optimized shapes is related to the periodic patterns in the initial designs, possibly because the employed periodic curved shape gets close to one of the numerous local minima of the design problem. For the twisting actuator, the optimization results depend less on the initial shape, possibly because the number of local minima is less. It is specially noted that, as shown by the third column in Fig. 12, even starting from a perfect hollow cylinder, the optimization still yields good results in all the three design problems, but at the expense of slower convergence rate. The proposed gradient-based optimization method cannot guarantee global minima, but it produces feasible solutions for soft robot design problems.

E. Robot Arm

In addition to basic actuation modes like linear motion, bending, and twisting as investigated above, shape morphing of soft robots in a general sense plays an important role in enabling locomotion and grasping functionalities [25], [39], [40]. In this example, we present design of soft robot arms that exhibit desired spatial configurations upon actuation. The robot arm is of a cylindrical shape with $r_0 = 10$ mm, $l_0 = 160mm$ and is fixed at one end. For such slender structures, the gravity exerts a considerable effect on the deformation behavior. Herein, we consider the robot arm placed horizontally at the initial undeformed state. The central axis is used to specify the spatial configuration of the robot arm, and it is expected

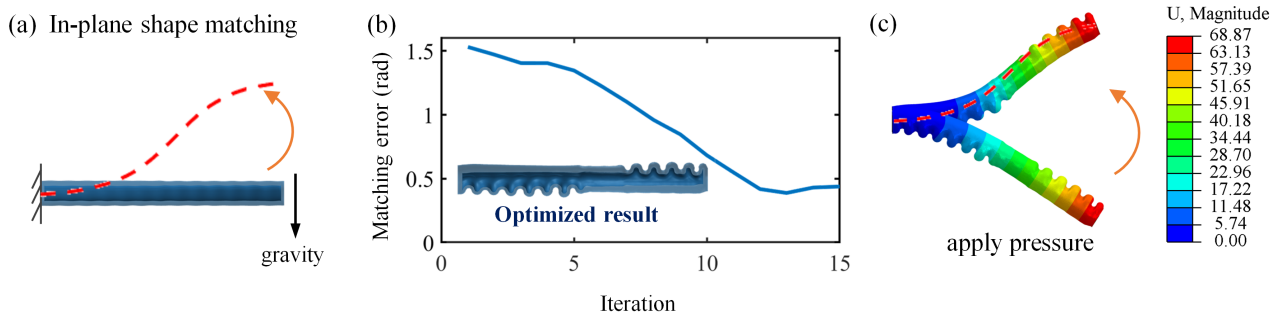

Fig. 13: In-plane shape matching: (a) the target shape, (b) the optimization history and the optimized design, and (c) the configuration change of the optimized design when the prescribed pressure is applied.

to deform into the target shapes that combine bends about multiple axes. Two user-defined target shapes are investigated: one in-plane curve, and one out-of-plane spatial curve.

The target curve is defined with a clamed B-spline curve. Then, ten equidistant cross sections are labelled along the lengthwise direction, each of which is attached with a coordinate system to describe its spatial orientation. The target shape to match in the optimization model is described by the sum of relative rotations of two adjacent sections, from the preceding section to the current section, which basically describes how the configuration navigates through space. Herein, the target is in fact a series of rotation matrices. The deformation performance of the actual deformed robot can be readily obtained in terms of the rotation matrices between adjacent sections. The difference of the target curve and the actual deformed curve in terms of the rotation matrices yields the shape matching error, which translates into a rotation axis vector and a rotation angle by the Rodrigues' rotation formula. Finally, the generalized adjoint force which is a moment here can be obtained, whose direction is aligned with the rotation axis vector and whose magnitude is proportional to the rotation angle.

1) In-plane Shape Matching: First, we investigate the in-plane shape matching problem. The target shape is two connected arcs with different directions of bending, as shown in Fig. 13(a). It is observed that, the orientation error keeps decreasing, as shown in Fig. 13(b). The optimized result plotted in the inset mainly includes two pieces of bending actuators that are naturally interconnected. We also observed that the robot arm tapers from the proximal to the distal end, which is caused by the gravitational effect since a tapered beam induces smaller bending moment generated by the distributed gravitational forces. This commonly exists in nature such as human fingers, elephant trunks, etc. [41]. The control points of the B-spline target curve are given in the supplementary table. The detailed exterior and interior shape information and the optimization process can be found in Movie S4.

Fig. 13(c) shows the configuration change of the optimized design from the initial state to the actuated state. It is found that, the initial design undergoes a considerable bending motion caused by the gravity. Upon actuation, the robot arm bends upwardly and the gravitational effect is compensated. Overall, it can be seen that the optimization result matches the desired target shape well along the full length of the robot. It is worthy of noting that, the target shape is created randomly and thus should not be expected to be matched perfectly.

2) Out-of-plane Shape Matching: Second, we investigate the out-of-plane shape matching problem. The target shape is several connected arcs with different directions of bending, as shown in Fig. 14(a). Also plotted are the projections of the spatial curve on $x-y$, $x-z$ and $y-z$ planes. It is observed that, the orientation error keeps decreasing, as shown in Fig. 14(b). The inset therein shows the optimized result in which bending features dominate and exhibit a continuous transition in terms of orientation along the lengthwise direction as an integral part. The control points of the B-spline target curve are given in the supplementary table. The detailed interior and exterior shape information and the optimization process can be found in Movie S4.

The robot arm with the spatial target shape is fabricated using the compound molding method, and Fig. 14(c) shows the experimental result of the deformed configuration of the optimized design, recorded by a camera from front, top and side views. It is observed that, the optimization result exhibits excellent repeatability upon pneumatic actuation, and matches well with the desired target shape along the full length of the robot.

IX. CO-OPTIMIZATION OF MULTIPLE CHAMBERS AND PRESSURES

In this section, we explore co-optimization of the morphological shape and the applied pressures of multiple chambers that can be employed to accommodate various operating conditions for pneumatic soft robots capable of complex tasks. It is noted that, a set of pressures as control variables are independently determined for each task by optimization, while the morphological shape evolution as structural variables must take into account all tasks by collecting the sensitivity information. Here, we study two cases to validate the effectiveness of the proposed method for addressing multi-target design problems: one using chambers in series to achieve multiple target curves, and another utilizing parallel chambers for multiple deformation modes.

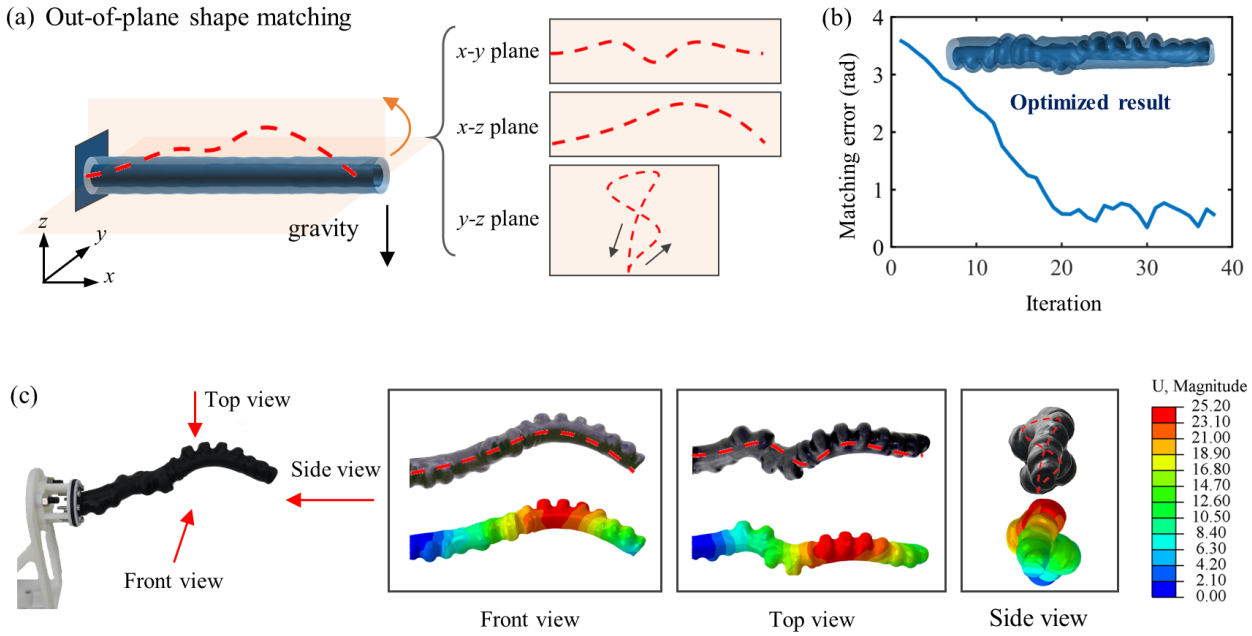

Fig. 14: Out-of-plane shape matching: (a) the target shape, (b) the optimization history and the optimized design, and (c) the configuration change of the optimized design when the prescribed pressure is applied.

A. Robot Arm with Chambers in Series

The first case extends the robot arm design as investigated in Section VIII-E to multiple chambers in series for the integration of deformation across multiple segments. As shown in Fig. 15(a), four air chambers in series are embedded inside the robot arm, aiming to match two different in-plane curves by concurrently optimizing the shape and the applied pressures. The dimension of the robot arm keeps the same as that in Section VIII-E. In addition to the exterior surface, four interior surfaces are involved and their sensitivities for the two target deformation profiles are calculated and summed with equal weights in each iteration. The effect of gravity is rigorously considered throughout the optimization.

It is observed that the matching errors in terms of orientation for both curves gradually decrease in the optimization process [see Fig. 15(b)], where the pressures of the four chambers are independently tailored for each task [see Fig. 15(c)]. To avoid unexpected self-contact and buckling phenomena, negative pressure is not explored in the optimization. The morphological evolution process is provided in Movie S5. The finite element analysis and experiments validate that the resulting deformations of both tasks match well with the target curves, with reference to Fig. 15(d). The morphology and pressure characteristics of the chambers play different roles in shaping the configuration of the robot arm. The morphology of the chambers governs the direction of bending, while the pressure tailors the magnitude of the bending curvature.

B. Robot Arm with Chambers in Parallel

The second case involves a robot arm initially deployed with four parallel air chambers, aiming to achieve bidirectional bending and twisting motions, drawing inspiration from [42]. The initial design, as depicted in Fig. 16(a), consists of a cylinder with dimensions $r_0 = 12$ mm and $l_0 = 100$ mm. The four chambers are positioned in parallel inside with dimensions $r_0 = 2.5$ mm and $l_0 = 94$ mm, and initial small shape perturbations are introduced for ease of shape evolution as in the cases above. Considering the symmetry of the problem, we set up two symmetric planes, i.e., $x-z$ plane and $y-z$ plane, where four chambers are symmetrically arranged and evolved.

In the optimization process, the morphological shape and the applied pressures iterate toward the target motion modes (with the weights of the three targets 1:1:3), as shown in Fig. 16(b). The pressure of each chamber is initialized to be 30 kPa and is allowed to vary between 0 and 60 kPa. The optimized design in Fig. 16(c) show that, a single chamber primarily contributes to the twisting motion while combination of different chambers may cancel out the twisting motion and lead to bending motions. Specifically, when the chambers on the same side are pressurized, the actuator bends in the opposite direction. When the diagonally opposite chambers are pressurized, the actuator undergoes twisting. In each motion mode, the optimized pressure reaches the limit, i.e., 0 or 60 kPa, as shown in Fig. 16(b). More detailed shape evolution process is provided in Movie S5. The finite element analysis and experiments validate the target deformation modes by varying the distributed air pressures [see Fig. 16(d)], in which the pressure of chamber B and C increases to 100 kPa when exhibiting the twisting motion.

Remark 6. An arbitrary target deformation is not guaranteed to be achieved since the design space spanned by the morphological shape and multiple pressure inputs is limited. It becomes more challenging to match multiple targets. Similar discussion was also made in [25]. More air inputs typically strengthen the capability of generating complex deformation,

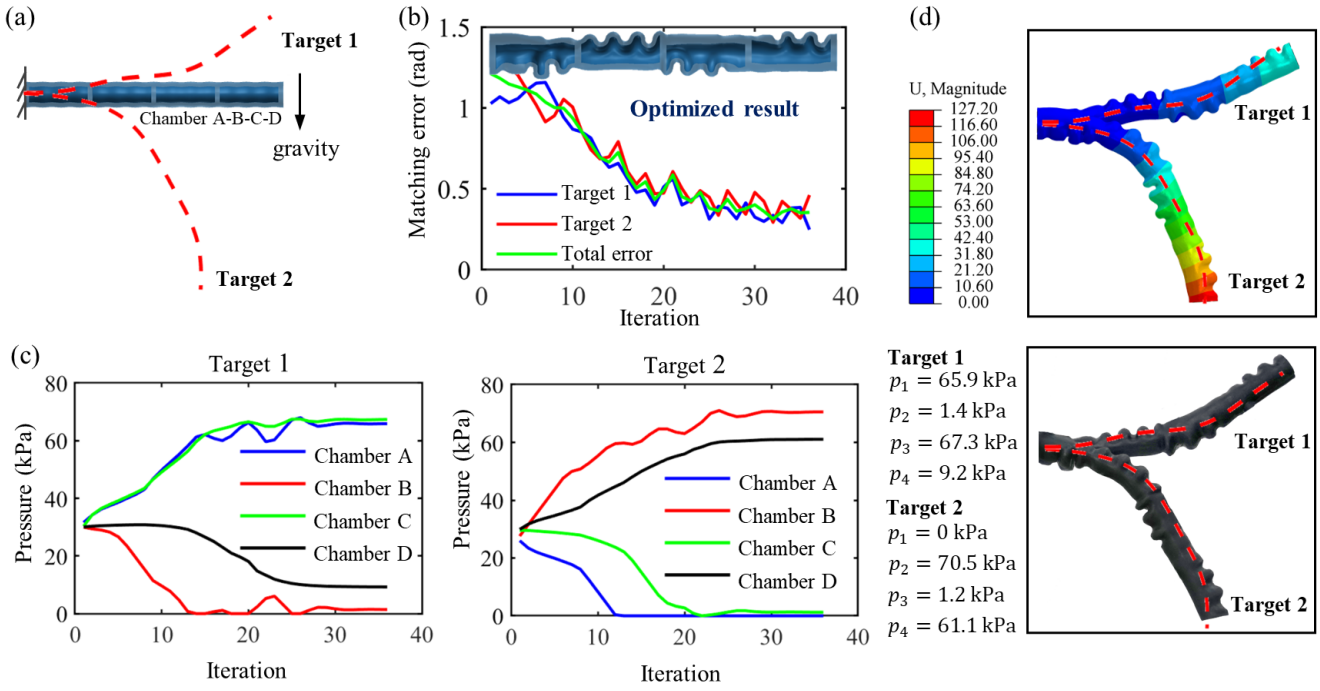

Fig. 15: Multiple chambers in series for multiple targets: (a) the robot arm deployed with four air chambers in series for matching the target in-plane deformation profiles, (b) the optimization history and the optimized design, (c) the optimization history of the applied pressures for the two tasks, and (d) the simulation and experiment results of configuration change of the optimized design when the prescribed pressures are applied.

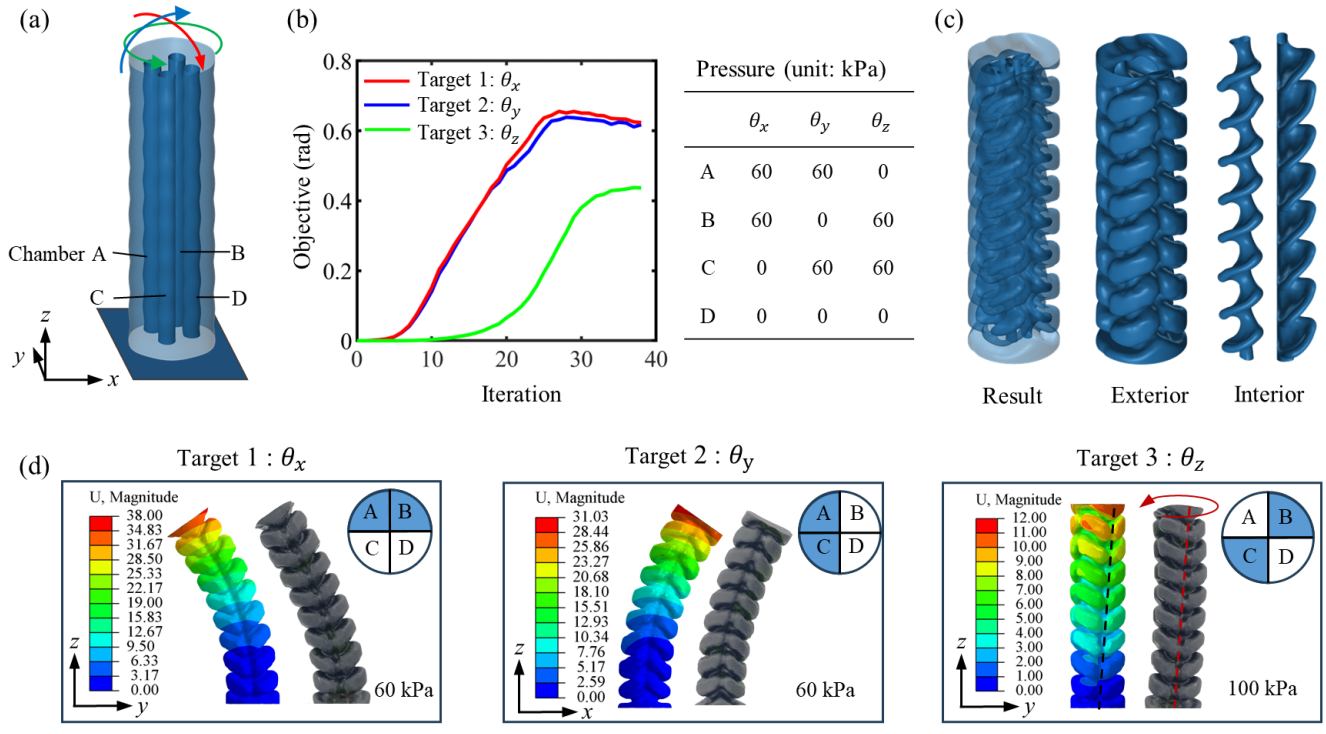

Fig. 16: Multiple chambers in parallel for multiple targets: (a) the robot arm deployed with four air chambers in parallel for bidirectional bending and twisting motions, (b) the optimization history and the resulting air pressures, (c) the optimized design, and (d) the simulation and experiment results of the motion modes of the optimized design when different pressure combinations are applied.

TABLE II: Computation statistics

	Linear actuator		Bending actuator		Twisting actuator		Robot arm		Multiple chamber	
	$k_{\text{eff}} = 0$	$4\,\text{N/mm}$	$k_{\text{eff}} = 0$	$100\,\text{N}\cdot\text{mm/rad}$	$k_{\text{eff}} = 0$	$400\,\text{N}\cdot\text{mm/rad}$	in-plane	out-of-plane	in series	in parallel
①	13650	13650	16338	16338	10962	10962	20205	20205	12464	25184
②	14	13	39	33	35	28	14	30	36	38
③	21'27"	18'31"	156'	82'6"	176'	80'46"	31'47"	97'19"	140'40"	358'53"
④	1'32"	1'25"	4'	2'29"	5'2"	2'53"	2'16"	3'14"	3'54"	9'27"
⑤	46%	44%	26%	40%	18%	27%	56%	49%	24%	23%
⑥	21%	20%	44%	30%	37%	21%	20%	35%	66%	41%
⑦	33%	36%	30%	30%	45%	52%	23%	15%	10%	36%

①: No. of control points ②: Iteration steps of optimization ③: Total time ④: Time per iteration step
⑤: Time of geometry model ⑥: Time of finite element analysis ⑦: Time of optimization
Primes indicate minutes, and double primes indicate seconds of time.

but in the meantime bring difficulty in fabrication and integration. It is still under-researched how to determine the minimal air chambers to realize the desired motion behaviors.

X. Discussion

A. Computation Statistics

In this work, all the numerical computation is performed on a computer with Intel Core i9-12900k processor (16 cores, 5.0 GHz) and 64 GB of RAM. We summarize in Table II the number of control points and the time consumptions of each case above. In most cases, it takes the largest part of time to perform optimization, since we update the geometric terms and their derivatives frequently for complying to the constraints. The time cost on nonlinear finite element analysis is the second largest. Specifically, the free motion analysis, i.e., $k_{\text{eff}} = 0$, incorporates larger deformation and thus requires more time. Besides, a larger number of control points are required for describing complex geometry, e.g., the robot arms, resulting in increased time spent on the geometry model, finite element analysis and optimization.

B. Advantages

The proposed morphological optimization method presents several distinct advantages in the context of soft robotics. First, it provides a systematic and rational method for inversely designing the morphological shape of pneumatic soft robots, by allowing simultaneous control of the interior and exterior shapes, such that the robot upon actuation evolves into the desired three dimensional configuration. In particular, the constraints of minimal distance and principal curvatures are well integrated in the optimization framework to guarantee the surface quality. Second, within a unified framework, the method offers an option to pursue balanced performance of deformation and load capability, by incorporation of the interacting stiffness which can be flexibly tailored by the designer. In addition, the proposed design approach is readily applicable to other hyperelastic material models, such as the Mooney-Rivlin model, the Gent model, etc.

C. Possible Extensions

Our design framework can be readily generalized to other geometric modelling approaches. In terms of theoretical sensitivity analysis, the sensitivity essentially relates the surface variation with respect to the motion behavior, and different geometric model only differs in the relationship between the surface variation and the geometric parameters. Due to the chain rule, one only needs to reconstruct this geometric relationship for a different model. The B-spline based surface employed in this work is topologically equivalent to cylindrical surfaces. One may also use enclosed surface modelling techniques, such as spherical harmonics [43] and parametric implicit surfaces. In addition, the isogeometric modelling approach [44] can be naturally combined with finite element method to improve the computational efficiency and inherently avoids the interpolation or mapping operation between different domains or mesh discontinuity, which is worthy of future research endeavor.

It is observed from the cases investigated in Section VIII that, some optimization results resemble shell structures, especially those with no interaction specifications, indicating a high degree of geometric similarity between the interior and exterior surfaces. In these cases, the combination of shell-based geometric modelling and FEA represents an alternative approach. Recently, Smith *et al.* explored shell-based FEA to replace volumetric FEA for simulation of thin-walled soft bodies, which allows for more prompt simulation results with little loss in accuracy [45]. One may optimize the shape of the shell structure and its thickness. This will significantly reduce the design parameter space and improve the computational efficiency.

D. Limitations

There are also some limitations in this work. First, we only consider shape optimization, i.e., the number of air chambers is prefixed. Although topology optimization that permits merging of geometric features is able to explore a more vast design space, the high dependency of the pressure load on the geometry will cause severe issues in both theory and computation. In general, each independent air chamber is expected to have an independent actuation pressure, and the chamber's shape and the pressure ought to be concurrently

optimized. However, the merging of different air chambers will cause discontinuity in the actuation pressure and the shape derivative, leading to numerical instability. Besides, the occurrence of very thin features during the emerging process may also bring difficulty in finite element analysis. One possible way to overcome the limitation of shape optimization is to optimize the number of chambers and their shapes simultaneously, i.e., a mixed optimization problem that contains both continuous and integer variables, which is beyond the scope of the present work. Second, the design is limited to geometric design only. Concurrent design of geometry and material represents a further step to explore the vast design space for modulating the deformation behavior and payload capabilities. It is also believed that, by integrated design that spans geometry, multiple actuations, and material domain, one may expect a soft robot to morph into various configurations which is desired for practical scenarios.

XI. Conclusion

In this article, we develop a mathematical optimization-based design approach to automatically shaping the interior and exterior morphology of soft robots that are pneumatically actuated. It is theoretically predicted by virtue of the first-order shape derivative how the embedded air chamber and the exterior profile of a pneumatic soft robot affect the large deformation behavior. Geometric constraints are well incorporated into the optimization framework to guarantee rational, smooth, and fair morphological shape. The requirement for load capability is also well considered by the interaction stiffness. Our method is substantiated with soft robotic applications, including design of actuators for basic extension, bending, and twisting motions, and continuous tapered robot arms that can perform desired in-plane and out-of-plane configurations. We also explore co-optimization of morphology and input pressures of multiple chambers to achieve multiple objectives.

In the future, we hope to combine morphological and multi-material design to further explore the design space. In a much expanded design space, better performance of soft robots is expected to perform diverse three dimensional configurations for complex tasks. One may also impart a higher level to the optimization model that incorporates the mapping from the configuration space to the task space, which will be an important step toward the end-to-end solution to design of soft robots.

Appendix A
B-spline Basis Function

Given a nondecreasing knot sequence $u_0, u_1, u_2, \ldots$, the B-spline of order 0 is defined by

$$B_{i,0}(u) = \begin{cases} 1 & u_i \le u \le u_{i+1} \\ 0 & \text{otherwise.} \end{cases} \tag{39}$$

The higher-order B-splines are defined by means of the Cox–de Boor recursion formula,

$$B_{i,d}(u) = \frac{u - u_i}{u_{i+d} - u_i} B_{i,d-1}(u) + \frac{u_{i+d+1} - u}{u_{i+d+1} - u_{i+1}} B_{i+1,d-1}(u). \tag{40}$$

Appendix B
Hyperelastic Material Model

The generalized Neo-Hookean model is adopted to characterize the material nonlinearity of silicone rubbers, with the free energy density expressed by,

$$W = \frac{\mu}{2}(\bar{I}_1 - 3) + \frac{\kappa}{2}(J-1)^2 \tag{41}$$

with $\bar{I}_1 = \text{trace}(\mathbf{F} \cdot \mathbf{F}^{\mathrm{T}}) J^{-2/3}$ being the first regulated invariant. The first Piola-Kirchhoff stress takes the following form

$$s_{ij} = \frac{\partial W}{\partial F_{ji}} = \mu\Big(\frac{1}{J^{2/3}} F_{ji} - \frac{1}{3}\bar{I}_1 F_{ij}^{-1}\Big) + \kappa J\big(J-1\big) F_{ij}^{-1} \tag{42}$$

where μ and κ are the shear modulus and bulk modulus of rubber at small strains.

Appendix C
Basic Geometric Quantities and Derivatives

$$\mathbf{r}_q = \sum_{i,j} \mathbf{P}_{ij} B_i^{q\prime} B_j^r, \mathbf{r}_r = \sum_{i,j} \mathbf{P}_{ij} B_j^q B_j^{r\prime} \tag{43}$$

$$\begin{gathered} \mathbf{r}_{qq} = \sum_{i,j} \mathbf{P}_{ij} B_i^{q''} B_j^r, \mathbf{r}_{qr} = \sum_{i,j} \mathbf{P}_{ij} B_j^{q'} B_j^{r'}, \\ \mathbf{r}_{rr} = \sum_{i,j} \mathbf{P}_{ij} B_i^q B_j^{r''} \end{gathered} \tag{44}$$

$$E = \mathbf{r}_q \cdot \mathbf{r}_q \tag{45a}$$
$$G = \mathbf{r}_r \cdot \mathbf{r}_r \tag{45b}$$
$$F = \mathbf{r}_q \cdot \mathbf{r}_r \tag{45c}$$
$$E_q = 2\mathbf{r}_q \cdot \mathbf{r}_{qq} \tag{46a}$$
$$E_r = 2\mathbf{r}_q \cdot \mathbf{r}_{qr} \tag{46b}$$
$$G_q = 2\mathbf{r}_r \cdot \mathbf{r}_{qr} \tag{46c}$$
$$G_r = 2\mathbf{r}_r \cdot \mathbf{r}_{rr} \tag{46d}$$

The second fundamental form of a surface $L, M, N(\mathbf{r}) \in \mathbb{R}$ is defined by

$$L = \mathbf{r}_{qq} \cdot \mathbf{m} \tag{47a}$$
$$N = \mathbf{r}_{rr} \cdot \mathbf{m} \tag{47b}$$
$$M = \mathbf{r}_{qr} \cdot \mathbf{m} \tag{47c}$$
$$m = \frac{\mathbf{r}_q \times \mathbf{r}_r}{\sqrt{EG - F^2}} \tag{48}$$

Their derivatives:

$$\frac{\partial \mathbf{r}}{\partial \mathbf{P}_{ij}} = B_i^q B_j^r \mathbf{I} \tag{49a}$$
$$\frac{\partial \mathbf{r}_q}{\partial \mathbf{P}_{ij}} = B_i^{q'} B_j^r \mathbf{I} \tag{49b}$$
$$\frac{\partial \mathbf{r}_r}{\partial \mathbf{P}_{ij}} = B_i^q B_j^{r'} \mathbf{I} \tag{49c}$$
$$\frac{\partial \mathbf{r}_{qq}}{\partial \mathbf{P}_{ij}} = B_i^{q''} B_j^r \mathbf{I} \tag{49d}$$
$$\frac{\partial \mathbf{r}_{qr}}{\partial \mathbf{P}_{ij}} = B_i^{q'} B_j^{r'} \mathbf{I} \tag{49e}$$
$$\frac{\partial \mathbf{r}_{rr}}{\partial \mathbf{P}_{ij}} = B_i^q B_j^{r''} \mathbf{I} \tag{49f}$$

where $B_i^{q'}$ and $B_i^{q''}$ the first-order and second order derivatives of the basis function, $\mathbf{I}$ is the unit tensor.

$$\frac{\partial E}{\partial \mathbf{P}_{ij}} = 2\mathbf{r}_q \cdot \frac{\partial \mathbf{r}_q}{\partial \mathbf{P}_{ij}} \tag{50}$$

$$\frac{\partial G}{\partial \mathbf{P}_{ij}} = 2\mathbf{r}_r \cdot \frac{\partial \mathbf{r}_r}{\partial \mathbf{P}_{ij}} \tag{51}$$

$$\frac{\partial F}{\partial \mathbf{P}_{ij}} = \mathbf{r}_q \cdot \frac{\partial \mathbf{r}_r}{\partial \mathbf{P}_{ij}} + \mathbf{r}_r \cdot \frac{\partial \mathbf{r}_q}{\partial \mathbf{P}_{ij}} \tag{52}$$

$$\frac{\partial E_q}{\partial \mathbf{P}_{ij}} = 2\left(\mathbf{r}_{qq} \cdot \frac{\partial \mathbf{r}_q}{\partial \mathbf{P}_{ij}} + \mathbf{r}_q \cdot \frac{\partial \mathbf{r}_{qq}}{\partial \mathbf{P}_{ij}}\right) \tag{53}$$

$$\frac{\partial E_r}{\partial \mathbf{P}_{ij}} = 2\left(\mathbf{r}_{qr} \cdot \frac{\partial \mathbf{r}_q}{\partial \mathbf{P}_{ij}} + \mathbf{r}_q \cdot \frac{\partial \mathbf{r}_{qr}}{\partial \mathbf{P}_{ij}}\right) \tag{54}$$

$$\frac{\partial G_q}{\partial \mathbf{P}_{ij}} = 2\left(\mathbf{r}_{qr} \cdot \frac{\partial \mathbf{r}_r}{\partial \mathbf{P}_{ij}} + \mathbf{r}_r \cdot \frac{\partial \mathbf{r}_{qr}}{\partial \mathbf{P}_{ij}}\right) \tag{55}$$

$$\frac{\partial G_r}{\partial \mathbf{P}_{ij}} = 2\left(\mathbf{r}_{rr} \cdot \frac{\partial \mathbf{r}_r}{\partial \mathbf{P}_{ij}} + \mathbf{r}_r \cdot \frac{\partial \mathbf{r}_{rr}}{\partial \mathbf{P}_{ij}}\right) \tag{56}$$

where $E_q, G_q(\mathbf{r}) \in \mathbb{R}$ denote the derivatives of first fundamental form of a surface.

$$\begin{aligned}\frac{\partial \mathbf{m}}{\partial \mathbf{P}_{ij}} = &\frac{1}{\sqrt{EG-F^2}}\left(\frac{\partial \mathbf{r}_q}{\partial \mathbf{P}_{ij}} \times \mathbf{r}_r - \frac{\partial \mathbf{r}_r}{\partial \mathbf{P}_{ij}} \times \mathbf{r}_q\right) \\ &- \frac{\mathbf{r}_q \times \mathbf{r}_r}{2\left(EG-F^2\right)^{\frac{3}{2}}}\left(G\frac{E}{\partial \mathbf{P}_{ij}} + E\frac{G}{\partial \mathbf{P}_{ij}} - 2F\frac{F}{\partial \mathbf{P}_{ij}}\right)\end{aligned} \tag{57}$$

$$\frac{\partial L}{\partial \mathbf{P}_{ij}} = \left(\frac{\partial \mathbf{r}_{qq}}{\partial \mathbf{P}_{ij}} \cdot \mathbf{m} + \mathbf{r}_{qq} \cdot \frac{\partial \mathbf{m}}{\partial \mathbf{P}_{ij}}\right) \tag{58}$$

$$\frac{\partial N}{\partial \mathbf{P}_{ij}} = \left(\frac{\partial \mathbf{r}_{rr}}{\partial \mathbf{P}_{ij}} \cdot \mathbf{m} + \mathbf{r}_{rr} \cdot \frac{\partial \mathbf{m}}{\partial \mathbf{P}_{ij}}\right) \tag{59}$$

$$\frac{\partial M}{\partial \mathbf{P}_{ij}} = \left(\frac{\partial \mathbf{r}_{qr}}{\partial \mathbf{P}_{ij}} \cdot \mathbf{m} + \mathbf{r}_{qr} \cdot \frac{\partial \mathbf{m}}{\partial \mathbf{P}_{ij}}\right) \tag{60}$$

APPENDIX D
CURVATURE

The mean curvature is

$$H = \frac{EN + GL - 2FM}{2\left(EG - F^2\right)}. \tag{61}$$

The Gaussian curvature is

$$K = \frac{LN - M^2}{EG - F^2}. \tag{62}$$

Their derivatives are as follows,

$$\begin{aligned}\frac{\partial H}{\partial \mathbf{P}_{ij}} = &\frac{N}{2\left(EG-F^2\right)}\frac{\partial E}{\partial \mathbf{P}_{ij}} + \frac{E}{2\left(EG-F^2\right)}\frac{\partial N}{\partial \mathbf{P}_{ij}} \\ &+ \frac{L}{2\left(EG-F^2\right)}\frac{\partial G}{\partial \mathbf{P}_{ij}} + \frac{G}{2\left(EG-F^2\right)}\frac{\partial L}{\partial \mathbf{P}_{ij}} \\ &- \frac{M}{EG-F^2}\frac{\partial F}{\partial \mathbf{P}_{ij}} - \frac{F}{EG-F^2}\frac{\partial M}{\partial \mathbf{P}_{ij}} \\ &- \frac{EN + GL - 2FM}{2\left(EG-F^2\right)^2}\left(E\frac{\partial G}{\partial \mathbf{P}_{ij}} + G\frac{\partial E}{\partial \mathbf{P}_{ij}} - 2F\frac{\partial F}{\partial \mathbf{P}_{ij}}\right)\end{aligned} \tag{63}$$

$$\begin{aligned}\frac{\partial K}{\partial \mathbf{P}_{ij}} = &\frac{N}{EG-F^2}\frac{\partial L}{\partial \mathbf{P}_{ij}} + \frac{L}{EG-F^2}\frac{\partial N}{\partial \mathbf{P}_{ij}} - \frac{2M}{EG-F^2}\frac{\partial M}{\partial \mathbf{P}_{ij}} \\ &- \frac{LN - M^2}{\left(EG-F^2\right)^2}\left(E\frac{\partial G}{\partial \mathbf{P}_{ij}} + G\frac{\partial E}{\partial \mathbf{P}_{ij}} - 2F\frac{\partial F}{\partial \mathbf{P}_{ij}}\right).\end{aligned} \tag{64}$$

APPENDIX E
COMPUTATION OF SURFACE VELOCITY

For point $\mathbf{x} = (x_1, x_2, x_3)$ in a quadratic tetrahedral element (C3D10H), the displacement field and the adjoint displacement field can be interpolated as

$$\mathbf{u}(\mathbf{x}) = N_i(\mathbf{x})\,\mathbf{U}^i \tag{65}$$

$$\mathbf{w}(\mathbf{x}) = N_i(\mathbf{x})\,\mathbf{W}^i \tag{66}$$

where $\mathbf{U}^i = \left(U_1^i, U_2^i, U_3^i\right)$ and $\mathbf{W}^i = \left(W_1^i, W_2^i, W_3^i\right)$ are the displacement and adjoint displacement of the i-th node $\mathbf{X}^i = (X_1, X_2, X_3)$, respectively, and N_i is the weight of the ith node which is a quadratic polynomial interpolation function in the following form

$$\begin{aligned}N_i(\mathbf{x}) = &a_i^1 + a_i^2 x_1 + a_i^3 x_2 + a_i^4 x_3 + a_i^5 x_1^2 + a_i^6 x_2^2 \\ &+ a_i^7 x_3^2 + a_i^8 x_1 x_2 + a_i^9 x_2 x_3 + a_i^{10} x_3 x_1\end{aligned} \tag{67}$$

with the coefficients determined by satisfying

$$N_i(\mathbf{X}^j) = \delta_{ij}, j = 1, ..., 10. \tag{68}$$

The deformation gradient and its partial derivative can be obtained,

$$F_{ij}(\mathbf{x}) = \delta_{ij} + \frac{\partial N_l(\mathbf{x})}{\partial x_j} U_i^l \tag{69}$$

$$\frac{\partial F_{ij}}{\partial x_k} = \frac{\partial^2 N_l(\mathbf{x})}{\partial x_j \partial x_k} U_i^l. \tag{70}$$

After obtaining the deformation gradient, (19) can be calculated at any point within the element. The stress $\mathbf{s}(\mathbf{u})$ can be computed based on the constitutive relation (42). The divergence term $\boldsymbol{\nabla} \cdot \left(J\mathbf{F}^{-1}\mathbf{w}\right)$ in (19) can be expressed by

$$\boldsymbol{\nabla} \cdot \left(J\mathbf{F}^{-1}\mathbf{w}\right) = F_{ij}^{-1} w_j \frac{\partial J}{\partial x_i} + J w_j \frac{\partial F_{ij}^{-1}}{\partial x_i} + J F_{ij}^{-1} \frac{\partial w_j}{\partial x_i} \tag{71}$$

with the following relations

$$\frac{\partial J}{\partial x_i} = \frac{1}{2}\epsilon_{pjk}\epsilon_{lmn}\frac{\partial F_{pl}}{\partial x_i} F_{jm} F_{kn} \tag{72}$$

$$\frac{\partial F_{ij}^{-1}}{\partial x_i} = -\frac{\partial F_{lk}}{\partial x_i} F_{il}^{-1} F_{kj}^{-1} \tag{73}$$

$$\frac{\partial w_j}{\partial x_i} = \frac{\partial N_l(\mathbf{x})}{\partial x_i} W_j^l \tag{74}$$

where ϵ_{lmn} is the permutation symbol.

REFERENCES

[1] D. Yang, B. Mosadegh, A. Ainla, B. Lee, F. Khashai, Z. Suo, K. Bertoldi, and G. M. Whitesides, "Buckling of elastomeric beams enables actuation of soft machines," *Advanced Materials*, vol. 27, no. 41, pp. 6323–6327, 2015.

[2] J. Kwon, S. J. Yoon, and Y.-L. Park, "Flat inflatable artificial muscles with large stroke and adjustable force–length relations," *IEEE Transactions on Robotics*, vol. 36, no. 3, pp. 743–756, 2020.

[3] Y. Cui, X.-J. Liu, X. Dong, J. Zhou, and H. Zhao, "Enhancing the universality of a pneumatic gripper via continuously adjustable initial grasp postures," *IEEE Transactions on Robotics*, vol. 37, no. 5, pp. 1604–1618, 2021.

[4] Y. Hao, S. Biswas, E. W. Hawkes, T. Wang, M. Zhu, L. Wen, and Y. Visell, "A multimodal, enveloping soft gripper: shape conformation, bioinspired adhesion, and expansion-driven suction," *IEEE Transactions on Robotics*, vol. 37, no. 2, pp. 350–362, 2020.

[5] G. Gu, N. Zhang, H. Xu, S. Lin, Y. Yu, G. Chai, L. Ge, H. Yang, Q. Shao, X. Sheng *et al.*, "A soft neuroprosthetic hand providing simultaneous myoelectric control and tactile feedback," *Nature Biomedical Engineering*, pp. 1–10, 2021.

[6] S. Puhlmann, J. Harris, and O. Brock, "Rbo hand 3: A platform for soft dexterous manipulation," *IEEE Transactions on Robotics*, vol. 38, no. 6, pp. 3434–3449, 2022.

[7] F. Chen and M. Y. Wang, "Design optimization of soft robots: A review of the state of the art," *IEEE Robotics and Automation Magazine*, vol. 27, no. 4, pp. 27–43, 2020.

[8] J. Hiller and H. Lipson, "Automatic design and manufacture of soft robots," *IEEE Transactions on Robotics*, vol. 28, no. 2, pp. 457–466, 2012.

[9] L.-K. Ma, Y. Zhang, Y. Liu, K. Zhou, and X. Tong, "Computational design and fabrication of soft pneumatic objects with desired deformations," *ACM Transactions on Graphics (TOG)*, vol. 36, no. 6, pp. 1–12, 2017.

[10] L. Ding, N. Dai, X. Mu, S. Xie, X. Fan, D. Li, and X. Cheng, "Design of soft multi-material pneumatic actuators based on principal strain field," *Materials & design*, vol. 182, p. 108000, 2019.

[11] F. Connolly, C. J. Walsh, and K. Bertoldi, "Automatic design of fiber-reinforced soft actuators for trajectory matching," *Proceedings of the National Academy of Sciences*, vol. 114, no. 1, pp. 51–56, 2017.

[12] S. Chen, F. Chen, Z. Cao, Y. Wang, Y. Miao, G. Gu, and X. Zhu, "Topology optimization of skeleton-reinforced soft pneumatic actuators for desired motions," *IEEE/ASME Transactions on Mechatronics*, vol. 26, no. 4, pp. 1745–1753, 2021.

[13] S. Chen, Y. Wang, D. Li, F. Chen, and X. Zhu, "Enhancing interaction performance of soft pneumatic-networks grippers by skeleton topology optimization," *Science China Technological Sciences*, vol. 64, no. 12, pp. 2709–2717, 2021.

[14] F. Chen, K. Liu, Y. Wang, J. Zou, G. Gu, and X. Zhu, "Automatic design of soft dielectric elastomer actuators with optimal spatial electric fields," *IEEE Transactions on Robotics*, vol. 35, no. 5, pp. 1150–1165, 2019.

[15] J. Tian, X. Zhao, X. D. Gu, and S. Chen, "Designing ferromagnetic soft robots (ferrosoro) with level-set-based multiphysics topology optimization," in *2020 IEEE International Conference on Robotics and Automation (ICRA)*. IEEE, 2020, pp. 10 067–10 074.

[16] R. Hashem, M. Stommel, L. K. Cheng, and W. Xu, "Design and characterization of a bellows-driven soft pneumatic actuator," *IEEE/ASME Transactions on Mechatronics*, vol. 26, no. 5, pp. 2327–2338, 2020.

[17] B. Mosadegh, P. Polygerinos, C. Keplinger, S. Wennstedt, R. F. Shepherd, U. Gupta, J. Shim, K. Bertoldi, C. J. Walsh, and G. M. Whitesides, "Pneumatic networks for soft robotics that actuate rapidly," *Advanced Functional Materials*, vol. 24, no. 15, pp. 2163–2170, 2014.

[18] G. Dämmer, S. Gablenz, A. Hildebrandt, and Z. Major, "Design and shape optimization of polyjet bellows actuators," in *2018 IEEE International Conference on Soft Robotics (RoboSoft)*. IEEE, 2018, pp. 282–287.

[19] G. Gu, D. Wang, L. Ge, and X. Zhu, "Analytical modeling and design of generalized pneu-net soft actuators with three-dimensional deformations," *Soft Robotics*, vol. 8, no. 4, pp. 462–477, 2021.

[20] C. Jiang, D. Wang, B. Zhao, Z. Liao, and G. Gu, "Modeling and inverse design of bio-inspired multi-segment pneu-net soft manipulators for 3d trajectory motion," *Applied Physics Reviews*, vol. 8, no. 4, p. 041416, 2021.

[21] D. Guo and Z. Kang, "Chamber layout design optimization of soft pneumatic robots," *Smart Materials and Structures*, vol. 29, no. 2, p. 025017, 2020.

[22] E. Siéfert, E. Reyssat, J. Bico, and B. Roman, "Bio-inspired pneumatic shape-morphing elastomers," *Nature materials*, vol. 18, no. 1, p. 24, 2019.

[23] F. Chen, Y. Miao, L. Zhang, S. Chen, and X. Zhu, "Triply periodic channels enable soft pneumatic linear actuator with single material and scalability," *IEEE Robotics and Automation Letters*, vol. 7, no. 2, pp. 2668–2675, 2022.

[24] F. Chen, Y. Miao, G. Gu, and X. Zhu, "Soft twisting pneumatic actuators enabled by freeform surface design," *IEEE Robotics and Automation Letters*, vol. 6, no. 3, pp. 5253–5260, 2021.

[25] G. Maloisel, E. Knoop, C. Schumacher, and M. Bächer, "Automated routing of muscle fibers for soft robots," *IEEE Transactions on Robotics*, vol. 37, no. 3, pp. 996–1008, 2021.

[26] B. Caasenbrood, A. Pogromsky, and H. Nijmeijer, "A computational design framework for pressure-driven soft robots through nonlinear topology optimization," in *2020 3rd IEEE International Conference on Soft Robotics (RoboSoft)*. IEEE, 2020, pp. 633–638.

[27] Y. Chen, Z. Xia, and Q. Zhao, "Optimal design of soft pneumatic bending actuators subjected to design-dependent pressure loads," *IEEE/ASME Transactions on Mechatronics*, vol. 24, no. 6, pp. 2873–2884, 2019.

[28] J. Guzman, A. Madureira, M. Sarkis, and S. Walker, "Analysis of the finite element method for the laplace–beltrami equation on surfaces with regions of high curvature using graded meshes," *Journal of Scientific Computing*, vol. 77, no. 3, pp. 1736–1761, 2018.

[29] G. E. Farin and G. Farin, *Curves and surfaces for CAGD: a practical guide*. Morgan Kaufmann, 2002.

[30] K. K. Choi and N.-H. Kim, *Structural sensitivity analysis and optimization 1: linear systems*. Springer Science & Business Media, 2006.

[31] T. Buhl, C. B. Pedersen, and O. Sigmund, "Stiffness design of geometrically nonlinear structures using topology optimization," *Structural and Multidisciplinary Optimization*, vol. 19, pp. 93–104, 2000.

[32] T. I. Vassilev, "Fair interpolation and approximation of b-splines by energy minimization and points insertion," *Computer-Aided Design*, vol. 28, no. 9, pp. 753–760, 1996.

[33] N. J. Lott and D. Pullin, "Method for fairing b-spline surfaces," *Computer-Aided Design*, vol. 20, no. 10, pp. 597–600, 1988.

[34] Y. Kineri, M. Wang, H. Lin, and T. Maekawa, "B-spline surface fitting by iterative geometric interpolation/approximation algorithms," *Computer-Aided Design*, vol. 44, no. 7, pp. 697–708, 2012.

[35] Z. Lin, Q. Shao, X.-J. Liu, and H. Zhao, "An anthropomorphic musculoskeletal system with soft joint and multifilament pneumatic artificial muscles," *Advanced Intelligent Systems*, vol. 4, no. 10, p. 2200126, 2022.

[36] D. Drotman, M. Ishida, S. Jadhav, and M. T. Tolley, "Application-driven design of soft, 3-d printed, pneumatic actuators with bellows," *IEEE/ASME Transactions on Mechatronics*, vol. 24, no. 1, pp. 78–87, 2018.

[37] Z. Jiao, C. Ji, J. Zou, H. Yang, and M. Pan, "Vacuum-powered soft pneumatic twisting actuators to empower new capabilities for soft robots," *Advanced Materials Technologies*, vol. 4, no. 1, p. 1800429, 2019.

[38] T. Jin, L. Li, T. Wang, G. Wang, J. Cai, Y. Tian, and Q. Zhang, "Origami-inspired soft actuators for stimulus perception and crawling robot applications," *IEEE Transactions on Robotics*, vol. 38, no. 2, pp. 748–764, 2021.

[39] S. Y. Kim, R. Baines, J. Booth, N. Vasios, K. Bertoldi, and R. Kramer-Bottiglio, "Reconfigurable soft body trajectories using unidirectionally stretchable composite laminae," *Nature communications*, vol. 10, no. 1, pp. 1–8, 2019.

[40] M. G. Atia, A. Mohammad, A. Gameros, D. Axinte, and I. Wright, "Reconfigurable soft robots by building blocks," *Advanced Science*, p. 2203217, 2022.

[41] T. McMahon, "Size and shape in biology," *Science*, vol. 179, no. 4079, pp. 1201–1204, 1973.

[42] J. I. Lipton, R. MacCurdy, Z. Manchester, L. Chin, D. Cellucci, and D. Rus, "Handedness in shearing auxetics creates rigid and compliant structures," *Science*, vol. 360, no. 6389, pp. 632–635, 2018.

[43] C. Brechbühler, G. Gerig, and O. Kübler, "Parametrization of closed surfaces for 3-d shape description," *Computer vision and image understanding*, vol. 61, no. 2, pp. 154–170, 1995.

[44] T. J. Hughes, J. A. Cottrell, and Y. Bazilevs, "Isogeometric analysis: Cad, finite elements, nurbs, exact geometry and mesh refinement," *Computer methods in applied mechanics and engineering*, vol. 194, no. 39-41, pp. 4135–4195, 2005.

[45] L. Smith, J. Haimes, and R. MacCurdy, "Stretching the boundary: Shell finite elements for pneumatic soft actuators," in *2022 IEEE 5th International Conference on Soft Robotics (RoboSoft)*. IEEE, 2022, pp. 403–408.

Feifei Chen (Member, IEEE) received the B.E. degree in mechanical engineering from University of Science and Technology of China, Hefei, China, in 2013, and the Ph.D. degree in mechanical engineering from National University of Singapore, Singapore, in 2018. He joined Shanghai Jiao Tong University, Shanghai, China, in 2018. He is currently an Associate Professor (tenure-track) with the School of Mechanical Engineering. His research interests have been focused on design theory and methods for soft robots. Dr. Chen is currently an Associate Editor for IEEE ROBOTICS & AUTOMATION MAGAZINE and IEEE ROBOTICS AND AUTOMATION LETTERS.

Zenan Song received the B.E. degree in vehicle engineering from Tongji University, Shanghai, China, in 2022. He is currently working toward the Ph.D. degree in mechanical engineering at Shanghai Jiao Tong University, Shanghai, China. His research interests include morphological design by optimization of soft robots.

Shitong Chen received the B.E. degree in aircraft design engineering from Xi'an Jiaotong University, Xi'an, China, in 2018. He is currently working toward the Ph.D. degree in mechanical engineering at Shanghai Jiao Tong University, Shanghai, China. His research interests include computational design of soft robots.

Guoying Gu (Senior Member, IEEE) received the B.E. degree (with honors) in electronic science and technology, and the Ph.D. degree (with honors) in mechatronic engineering from Shanghai Jiao Tong University, Shanghai, China, in 2006 and 2012, respectively. Since 2012, he has worked with Shanghai Jiao Tong University, where he is currently appointed as a Professor of School of Mechanical Engineering. He has authored or coauthored of more than 90 publications, which have appeared in Science Robotics, Science Advances, IEEE/ASME Trans., Advanced Functional Materials, Soft Robotics, etc., as book chapters and in conference proceedings. His research interests include soft robotics, bioinspired and wearable robots, smart materials sensing, actuation and motion control.

Dr. Gu was a Humboldt Fellow with University of Oldenburg, Germany. He was a Visiting Scholar with Massachusetts Institute of Technology, National University of Singapore and Concordia University. He was a recipient of the National Science Fund for Distinguished Young Scholars in 2020. He currently serves as an Associate Editor for IEEE TRANSACTIONS ON ROBOTICS and IEEE ROBOTICS AND AUTOMATION LETTERS. He has also served for several journals as Editorial Board Member, Topic Editor, or Guest Editor, and several international conferences/symposiums as Chair, Co-Chair, Associate Editor or Program Committee Member.

Xiangyang Zhu (Member, IEEE) received the B.S. degree in automatic control from Nanjing Institute of Technology, Nanjing, China, in 1985, the M.Phil. degree in instrumentation engineering, and the Ph.D. degree in control engineering, both from Southeast University, Nanjing, China, in 1989 and 1992, respectively. From 1993 to 1994, he was a Postdoctoral Research Fellow with Huazhong University of Science and Technology, Wuhan, China. He joined the Department of Mechanical Engineering, Southeast University, as an Associate Professor in 1995. Since 2002, he has been with the School of Mechanical Engineering, Shanghai Jiao Tong University, Shanghai, China, where he is currently a chair Professor and the Director of the Robotics Institute. He has authored or coauthored more than 200 papers in international journals and conference proceedings. His research interests include robotic manipulation planning, neuro-interfacing and neuro-prosthetics, and soft robotics.

Dr. Zhu was a recipient of a number of awards including the National Science Fund for Distinguished Young Scholars from NSFC in 2005, and the Cheung Kong Distinguished Professorship from the Ministry of Education in 2007. He currently serves on the editorial board for IEEE TRANSACTIONS ON CYBERNETICS AND BIO-DESIGN AND MANUFACTURING.